
White Rose Research Online

eprints@whiterose.ac.uk
https://eprints.whiterose.ac.uk
Universities of Leeds, Sheffield and York

Deposited via The University of Sheffield.

White Rose Research Online URL for this paper:
https://eprints.whiterose.ac.uk/id/eprint/247769/

Version: Published Version

Article:
Gillan, A.F., Wyrzykowski, Ł, Mikołajczyk, P.J. et al. (2026) Time-domain photometry and activity evolution of interstellar comet 3I/ATLAS with BHTOM. Astronomy & Astrophysics, 714. A258. ISSN: 0004-6361

https://doi.org/10.1051/0004-6361/202659913

Reuse
This article is distributed under the terms of the Creative Commons Attribution (CC BY) licence. This licence allows you to distribute, remix, tweak, and build upon the work, even commercially, as long as you credit the authors for the original work. More information and the full terms of the licence here: https://creativecommons.org/licenses/

Takedown
If you consider content in White Rose Research Online to be in breach of UK law, please notify us by emailing eprints@whiterose.ac.uk including the URL of the record and the reason for the withdrawal request.





A&A, 714, A258 (2026)
https://doi.org/10.1051/0004-6361/202659913
© The Authors 2026

Astronomy & Astrophysics

Time-domain photometry and activity evolution of interstellar comet 3I/ATLAS with BHTOM

A. Fraser Gillan[1,⋆], Łukasz Wyrzykowski[1,2,3], Przemysław J. Mikołajczyk[4,1], Krzysztof Kotysz[4,2], Erica Bufanda[5], Colin O. Chandler[6,7,8], Süleyman Fişek[9,10], Henry H. Hsieh[11], Michael S. P. Kelley[12], Priscila J. Pessi[1], James E. Robinson[5], Sinan Aliş[9,10], Wieńczysław Bykowski[13,3], Richard E. Cannon[5], Martin Dominik[14], Barbara Handzlik[15], Mehmet İçen[9], Sebastian Kurowski[15], Ahmet Cem Kutluay[16,17,18], Joysankar Majumdar[2], Çağlayan Nehir[19], David O'Neill[20], Sibel Ötken[9], Kangming Pu[21], Özlem Şimşir[17,18], Colin Snodgrass[5], Cihan Tuğrul Tezcan[22], Fatma Tezcan[23], Mauritz Wicker[2,24], Fuat Korhan Yelkenci[9], Michał Żejmo[25], Kendall Ackley[26], Michael Andersen[27], Catalina Ávalos-Vega[28], Sergey Belkin[21], Valerio Bozza[29,30], Rene P. Breton[31], Martin J. Burgdorf[32], Jorge Casares[33], Vik Dhillon[34], Abbie Donaldson[5], Martin J. Dyer[34], Roberto Figuera Jaimes[35,36,37,14], Duncan K. Galloway[21], Tobias C. Hinse[38], Markus Hundertmark[39], Elahe Khalouei[40], Thomas Killestein[26], Rubina Kotak[41], Amit Kumar[42,26], Feng-Yuan Frey Liu[5], Penelope Longa-Peña[28], Joe Lyman[26], Luigi Mancini[43,44], Ayush Moharana[16], Valeska Molina[35], Kanthanakorn Noysena[45], Laura Kate Nuttall[46], Paul O'Brien[47], Vincent Okoth[5], Cyrielle Opitom[5], Don Pollacco[26], Markus Rabus[48], Gavin Ramsay[49], Sedighe Sajadian[50,51], A. Salinas San Martin[35], Jesper Skottfelt[42], John Southworth[16], Danny Steeghs[26], Jeremy Tregloan-Reed[28], Krzysztof Ulaczyk[26], and Roberta Vieliute[14,24]

(Affiliations can be found after the references)

Received 17 March 2026 / Accepted 3 August 2026

ABSTRACT

Context. Time-domain photometric monitoring is essential for characterizing cometary evolution, particularly for rare interstellar objects with limited observing opportunities.

Aims. We aimed to characterize the pre-perihelion photometric behavior and dust activity of the interstellar comet 3I/ATLAS and to test the capability of the Black Hole Target and Observation Manager (BHTOM) platform and telescope network for coordinated high-cadence non-sidereal observations.

Methods. We obtained 70 days of time-series photometry of 3I/ATLAS from 2025 July 4 to September 11 using 16 telescopes and 1554 images. The data were processed and calibrated with the BHTOM pipeline. High-cadence multiband imaging was used to measure the rotation period and color evolution, while the dust activity was quantified via $Af\rho$ measurements.

Results. We present a pre-perihelion light curve of 3I/ATLAS from R_h = 3.18–2.19 au, which exhibited a steady brightening by ∼3 magnitudes with no evidence of anomalous behavior. We measured a rotation period of $P_{\rm rot}$ = 15.98 ± 0.08 h. The colors were statistically non-changing, with only a weak, non-significant tendency for 3I/ATLAS to become bluer at $3.5 > R_h > 2.2$ au. The relative dust production increased from $A(0°)f\rho$ ∼600 to 1100 cm, and the upper limit on the dust mass-loss rate increased from ≤217 kg s^{-1} to ≤328 kg s^{-1}. We measured an activity index of $n = -1.24 \pm 0.02$, which is consistent with a well-developed dust coma.

Key words. methods: observational – techniques: image processing – techniques: photometric – telescopes – comets: general – comets: individual: 3I/ATLAS

1. Introduction

To date, three interstellar objects (ISOs) on unbound, hyperbolic orbits have been discovered. The first, 1I/'Oumuamua (Meech et al. 2017b; Williams et al. 2017), was identified on 2017 October 19 by the Panoramic Survey Telescope and Rapid Response System (Pan-STARRS) survey (Chambers et al. 2016). Notably, 1I/'Oumuamua exhibited no apparent coma (Jewitt et al. 2017) but displayed non-gravitational acceleration consistent with comet-like outgassing (Micheli et al. 2018). The second ISO, 2I/Borisov, discovered on 2019 August 30, showed clear cometary activity and spectral properties similar to those of typical Solar System comets (Fitzsimmons et al. 2019; Jewitt & Luu 2019; Opitom et al. 2019; Guzik et al. 2020; Fitzsimmons et al. 2024). The third known ISO, 3I/ATLAS, was discovered on UT 2025 July 1 (Denneau et al. 2025) by the Asteroid Terrestrial-impact Last Alert System (ATLAS; Tonry et al. 2018b) survey's Chilean unit.

Early observations quickly confirmed the cometary nature of 3I/ATLAS. Independent reports of activity were published by Alarcon et al. (2025), Jewitt & Luu (2025a), and Minev et al. (2025), while a series of follow-up studies further characterized the physical properties (see Frincke et al. 2026 and references therein for a further detailed overview). Multiband imaging and spectroscopy revealed that 3I/ATLAS is redder than most Solar System comets (Belyakov et al. 2025; Bolin et al. 2025; Champagne et al. 2025; de la Fuente Marcos et al. 2025; Kareta et al. 2025; Opitom et al. 2025; Seligman et al. 2025; Xing et al. 2025; Yang et al. 2025). Xing et al. (2025) also detected the first

⋆ Corresponding author.

Open Access article, published by EDP Sciences, under the terms of the Creative Commons Attribution License (https://creativecommons.org/licenses/by/4.0), which permits unrestricted use, distribution, and reproduction in any medium, provided the original work is properly cited.
This article is published in open access under the Subscribe to Open model. Subscribe to A&A to support open access publication.

evidence of water activity in 3I/ATLAS at a heliotric distance of 2.9 au, while Cordiner et al. (2025) and Lisse et al. (2025) showed a high CO_2 production rate with a high CO_2/H_2O ratio.

Chandler et al. (2026) presented results from the 8.4 m Simonyi Survey Telescope at the NSF–DOE Vera C. Rubin Observatory (Ivezić et al. 2019) based on 97 images obtained in multiple filters. The analysis presented in Chandler et al. (2026) provided astrometry, photometry, and morphological characterization of the comet's activity between UT 2025 June 21 and UT 2025 July 7. The study measured a lower-limit V-band absolute magnitude of $H_V = (13.32 \pm 0.16)$ mag, and an equivalent upper-limit effective nuclear radius of $r_n \sim (6.6 \pm 0.5)$ km. Jewitt et al. (2025) estimated a smaller radius upper limit of $r_n \leq 2.8$ km using a fit to the surface brightness profile measured from Hubble Space Telescope observations. When adopting the smaller radius estimate, the nucleus of 3I/ATLAS is larger than both 1I/'Oumuamua (Meech et al. 2017b; Fitzsimmons et al. 2018) and 2I/Borisov (Guzik et al. 2020; Jewitt et al. 2020).

The dynamical properties of 3I/ATLAS have also been investigated. Using the Ōtautahi-Oxford model (Hopkins et al. 2025a), Hopkins et al. (2025b) ruled out the scenario that 3I/ATLAS originated in the same star system as both 1I/'Oumuamua and 2I/Borisov. From analysis of the velocity, 3I/ATLAS appears to have originated from the Milky Way's thick disk, making it the first ISO identified from this region.

Comet 3I/ATLAS reached perihelion on UT 2025 October 29 at a heliocentric distance of $q = 1.36$ au, according to JPL Horizons (Giorgini et al. 1996). The ISO entered solar conjunction in mid-October and reappeared in November 2025; ground-based observations were therefore concentrated in the pre-perihelion interval, in the weeks leading up to solar conjunction. This paper presents high-cadence photometric measurements and analysis of 3I/ATLAS prior to solar conjunction using 16 different telescopes, distributed worldwide in both the northern and southern hemispheres. We followed the evolution of the brightness, dust production and color from 2025 July 04, three days after discovery, to 2025 September 11, and we simultaneously tested the capabilities of the Black Hole Target and Observation Manager (BHTOM) for non-sidereal objects.

2. BHTOM and observations

2.1. BHTOM

Time-domain astronomy is driven by the current wide-field surveys such as ATLAS (Tonry et al. 2018b), Pan-STARRS (Chambers et al. 2016), and ZTF (Bellm et al. 2019). This approach has become essential for studying astrophysical phenomena across a wide range of timescales, from rapidly evolving objects to long-term evolution. The Legacy Survey of Space and Time (LSST; Ivezić et al. 2019) conducted by the Vera C. Rubin Observatory will reach much fainter objects than current sky surveys and is expected to revolutionize transient astrophysics by finding thousands of new events every single night and discovering an order of magnitude more objects in each of the Solar System's small body reservoirs (Schwamb et al. 2023). However, these surveys typically follow fixed cadences and revisit sky-fields every few days to weeks, often in different filters, making high-cadence, single-filter monitoring challenging. BHTOM[1] (Wyrzykowski 2024; Mikolajczyk et al. 2025) provides an effective complement to survey-based data. The system and its associated telescope network were created in 2013 with the main purpose of the follow-up of alerts from ESA's Gaia Space Mission (Hodgkin et al. 2021). BHTOM is not an alert broker; rather, it is the missing link between brokers and the telescopes. BHTOM is an open-source platform that employs a uniform, automated pipeline designed to deliver science-ready photometry. It is based on the Target and Observation Manager (TOM) open-source framework developed by the Las Cumbres Observatory (Street et al. 2018). BHTOM enables user-defined observation requests for targeted, high-cadence photometric monitoring of individual objects. BHTOM currently accepts requests for targets for long-term or rapid photometric monitoring, such as transients, microlensing events, quasars, variable stars, and extrasolar planets. At the time of writing, the BHTOM telescope network is made up of ~170 telescopes worldwide and includes robotic, manual, amateur, and professional facilities, with mirror diameters ranging from 0.03 m to 2.5 m.

Users can upload reduced data (bias-, dark-, and flat-field–corrected) from both charge-coupled device (CCD) and complementary metal–oxide–semiconductor (CMOS) cameras to BHTOM, enabling observers beyond the professional community, such as amateur astronomers and school pupils, to contribute. All observations are then automatically processed and standardized in BHTOM in order to provide calibrated science-ready data. Automatic calibration of CCD and CMOS images is performed using a combination of established software packages, including CCDPhot (Wyrzykowski 2024; Mikolajczyk et al. 2025), Source-Extractor (SExtractor; Bertin & Arnouts 1996), Software for Calibrating AstroMetry and Photometry (SCAMP; Bertin 2006), Dominion Astrophysical Observatory Photometry (DAOPHOT II; Stetson 1987), and WCSTools.[2] Calibration in BHTOM is performed using Gaia Synthetic Photometry (GaiaSP; Gaia Collaboration 2023a) derived from the Gaia XP low-resolution spectra, in which the Gaia G bandpass (350–1050 nm, Weiler 2018) is decomposed and integrated through the desired bandpasses. This provides color-corrected synthetic magnitudes appropriate for point-spread function (PSF) photometry. A PSF model is constructed automatically for each image, and stellar and target fluxes are measured using PSF fitting. The photometric uncertainty assigned to each measurement is taken from the formal PSF-fitting error returned by DAOPHOT II, which reflects the noise properties of the image and the quality of the PSF model fit (Stetson 1987). These uncertainties, therefore, capture both photon noise and fitting residuals and provide an appropriate estimate of the measurement precision for each data point.

The astrometric solution is derived using reference catalogs, including the U.S. Naval Observatory (USNO) Robotic Astrometric Telescope (URAT-1; Zacharias et al. 2015), the fourth United States Naval Observatory (USNO) CCD Astrograph Catalog (UCAC-4; Zacharias et al. 2013), the United States Naval Observatory B1.0 Catalog (USNO-B1.0; Monet et al. 2003), and Gaia-DR3 (Gaia Collaboration 2023a). Photometric calibration is standardized to magnitudes based on GaiaSP (Gaia Collaboration 2023 b) and the Two Micron All Sky Survey (2MASS; Skrutskie et al. 2006) reference catalogs. A detailed description of the BHTOM system, including the data processing and automation architecture, is provided in Mikolajczyk et al. (2025). Finally, BHTOM combines processed input images with all available archival photometry to produce the most complete calibrated light curves possible.

[1] https://bhtom.space

[2] http://tdc-www.harvard.edu/wcstools/

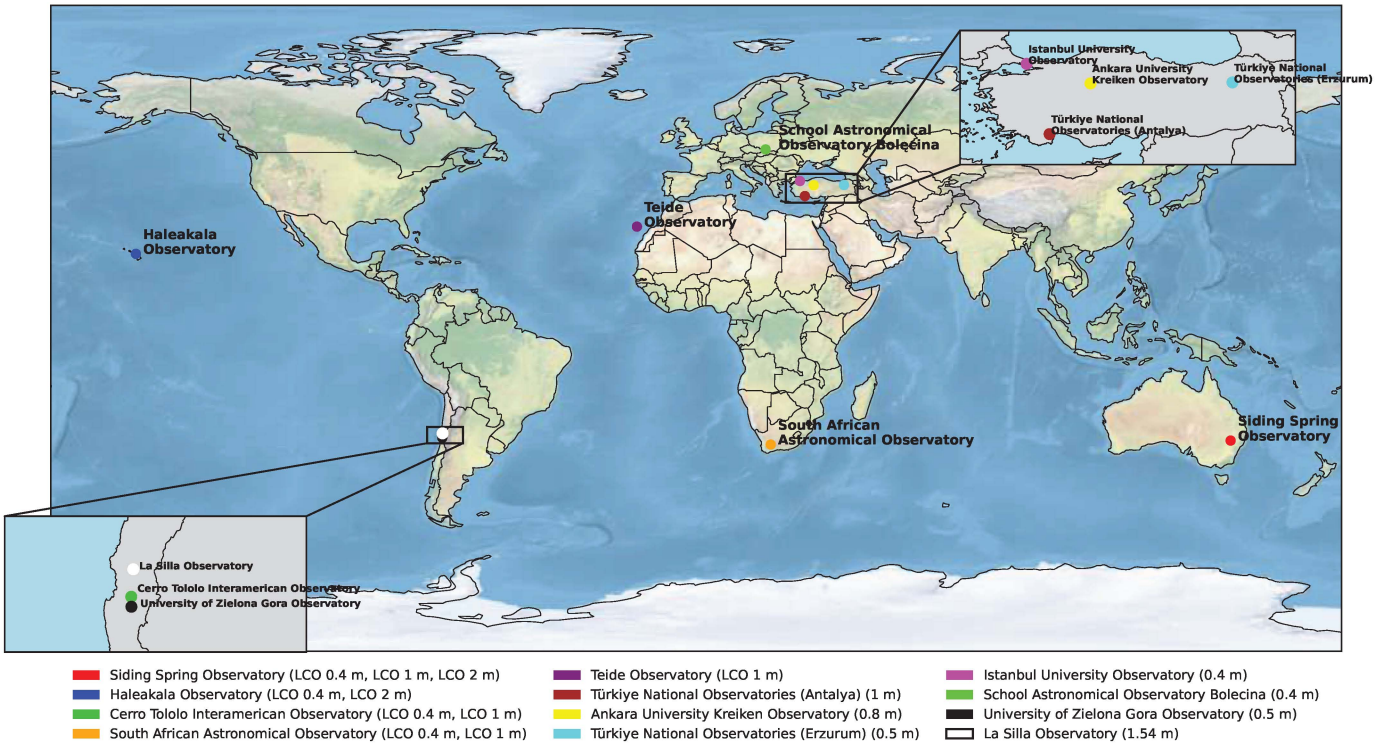


Fig. 1. Geographic locations of the observatories from which photometric data were obtained. Colors correspond to observatory names, and telescope apertures are given in the legend. Insets indicate regions with clustered sites.

2.2. BHTOM and the Solar System

BHTOM currently supports observation requests for non-Solar System targets, as described in Section 2.1. The core observing-network and data-processing functionality used in this work was already available within BHTOM. Ongoing development is extending this functionality into a dedicated Solar System workflow built around these existing capabilities, allowing non-sidereal targets such as comets and asteroids to be handled more directly within the platform. Planned functionality includes the ability to generate ephemerides; submit observation requests for comets and asteroids within a defined observing window; query archival data for past observations of the requested target, ultimately providing a light curve for any Solar System object; coordinate future observing campaigns; and enable rapid follow-up observations in response to alerts from surveys, brokers, or community triggers, without the requirement for telescope proposals.

In this work, 3I/ATLAS was handled using the existing BHTOM framework through an interim approach rather than through a dedicated Solar System interface. Each observation was treated as a separate target for the purposes of image processing, and the resulting measurements were then combined to produce the final light curve. Although the dedicated Solar System workflow is not yet publicly available, these observations demonstrate the ability of the BHTOM observing network and data-processing framework to support work on a fast-moving Solar System small body in support of future non-sidereal observations.

2.3. Observations

The following subsections describe the individual observatories and telescope facilities that contributed data to this study. We used data from both our own allocated observing time with the Las Cumbres Observatory Global Telescope (LCOGT) network facilities, and a variety of observatories that have contributed data using the BHTOM network. The resulting observation log is shown in Table A.1, which summarizes all observatories, telescopes, filters, the number of exposures, and the range of observation dates. The dataset combines measurements from both northern and southern hemisphere observatories, providing broad temporal and geographic coverage. In this work, BHTOM was used to (1) coordinate follow-up observations from telescopes within its network, after the target was circulated to participating observatories, and to (2) process the resulting images through its photometric pipeline. All photometry (with the exception of the GOTO data) was performed consistently using the BHTOM photometry pipeline as described in Section 2.1 to ensure consistency across sites. In this work we used a total of 1554 images for detailed analysis. Figure 1 shows the locations of the contributing observatories.

2.3.1. The LCOGT network

The LCOGT network maintains a globally distributed, multi-aperture robotic telescope network (Brown et al. 2013). We obtained data from five observatories in the network, using 0.4 m telescopes at Siding Spring Observatory in Australia, the South African Astronomical Observatory (SAAO), Cerro Tololo Inter-American Observatory (CTIO) in Chile, and Haleakala Observatory in Hawaii, and 1.0 m telescopes at Siding Spring Observatory, SAAO, CTIO, and Teide Observatory in the Canary Islands. The observations were obtained between UT 2025 July 5 and UT 2025 September 11 using both the 0.4 m and 1 m facilities across these sites, see Table A.1. The 0.4 m and 1 m telescopes have the same design across all sites, where the 0.4 m telescopes are PlaneWave Delta Rho 350 telescopes equipped with QHY600

CMOS cameras which provide $30' \times 30'$ fields of view (FOVs) with pixel scales of approximately 0.″74/pixel. Meanwhile, the 1 m telescopes are equipped with Sinistro cameras with $13' \times 13'$ FOVs with pixel scales of 0.″78/pixel with 2×2 binning in central 2k×2k readout mode. These telescopes used the Sloan g', r', and i' filters with central wavelengths 4770 Å, 6215 Å, and 7545 Å, respectively. All of the observations from the LCOGT network were automatically reduced using the Beautiful Algorithms to Normalize Zillions of Astronomical Images (BANZAI) pipeline (McCully et al. 2018). Depending on the telescope and lunar elongation angle, we used 30, 40, or 45 second exposures to minimize trailing effects.

2.3.2. School Astronomical Observatory Bolęcina

The School Astronomical Observatory Bolęcina (SOAB), located in southern Poland, operates a 0.4 m telescope equipped with a CMOS camera with a pixel scale of 0.238″/pixel, providing a field of view of $19.3' \times 12.6'$. Data were collected over three nights: 2025 July 04, 2025 July 20 and 2025 July 23, with a total of 13 images, see Table A.1. Observations were obtained using the Johnson-Cousins (hereafter J-C) R and I filters, with individual exposures of 300 seconds for R-band and 120 seconds for I-band. To mitigate short-timescale scatter and improve the signal-to-noise ratio of the SOAB data, the calibrated photometry was binned in time using 0.5-day intervals. We combined the measurements within each 0.5-day bin in flux space by converting magnitudes to fluxes, computing the weighted-mean flux, and converting back to a magnitude. For these magnitude–flux conversions, we used zero-points calibrated for the Johnson-Cousins $UBVRI$ system in the Vega magnitude scale (Gaia Collaboration 2023a). The corresponding zero-points were obtained from the Vega stellar spectrum as presented by Bessell & Murphy (2012). The same zero-point was used consistently in both the magnitude-to-flux and flux-to-magnitude conversions. The binning used inverse-variance weighting, with 3σ clipping applied – only if four or more measurements were present within a bin. The reported uncertainties correspond to the larger of the weighted-mean uncertainty and the intra-bin scatter.

2.3.3. Observations with Turkish telescopes

We observed 3I/ATLAS using four different telescopes across Türkiye. At the Türkiye National Observatories in Antalya, we used the 1 m TUG100 telescope on UT 2025 July 11. This telescope is equipped with a 4k × 4k CCD detector, providing a $21.5' \times 21.5'$ FOV and a pixel scale of 0.″31/pixel. We used the Sloan r', i', and z' filters with 2×2 on-chip binning and individual exposure times of 60 seconds. These photometric measurements were combined into a single-night bin, per filter, to maximize the signal-to-noise ratio.

We also used the 0.8 m T80 telescope at the Ankara University Kreiken Observatory to observe 3I/ATLAS on UT 2025 July 7. The instrument is equipped with a 1k × 1k CCD detector, providing a $12' \times 12'$ FOV with a pixel scale of 0.″69/pixel. Observations were made using the g', r', and i' filters, with 2×2 on-chip binning. A total of 50 images were taken with exposure times between 30 and 90 seconds. The photometric measurements were then binned by night, per filter, resulting in three data points.

We used the 0.5 m ATA050 telescope at the Erzurum site of Türkiye National Observatories on UT 2025 July 7. This telescope is equipped with a QHY268M CMOS camera which provided a $20' \times 14'$ FOV and a pixel scale of 0.″19/pixel. Observations were performed without a photometric filter (i.e., clear) and using 4×4 on-chip binning with individual exposure times of 90 seconds. A total of nine images were taken, and the resulting photometric measurements were subsequently combined into a single-night bin. The clear-filter measurements were calibrated to the J–C R-band using the BHTOM pipeline.

Finally, we used the 0.4 m IST40 telescope at the Istanbul University Observatory on six nights between UT 2025 July 18 and UT 2025 July 27. This telescope has a 3358×2536 CCD detector, giving a $15.5' \times 11.5'$ field of view and a pixel scale of 0.″27/pixel. These observations were also performed without a photometric filter (clear) with individual exposure times of 90 seconds. All images were acquired using 4×4 on-chip binning, and the resulting photometric measurements were then binned by night to maximize the signal-to-noise ratio. These images were calibrated to the J–C R-band using the BHTOM pipeline. All measurements that were binned in flux, similarly to the SOAB data in Section 2.3.2, are highlighted in Table A.1.

2.3.4. University of Zielona Góra Observatory

The University of Zielona Góra Observatory (UZO) hosts a 0.5 m telescope, located at the Deep Sky Chile site in the Rio Hurtado Valley, Chile. We observed 3I/ATLAS on five nights between UT 2025 July 17 and 2025 July 24. The telescope uses a 26 megapixel QHY268M Pro CMOS camera with a pixel scale of 0.″23/pixel and a field of view of $23' \times 15'$. Each of the observations taken with this telescope were 60 second exposures, taken sequentially in the J-C B, V and R bands, see Figure 4a. These images were the highest cadence in this study, with a total of 656 images taken over the five nights.

2.3.5. The Danish 1.54-metre telescope

We used the Danish 1.54 m telescope (D154T) at La Silla Observatory in Chile on three nights between 2025 July 16 and 2025 July 29. The D154T was equipped with the Danish Faint Object Spectrograph and Camera (DFOSC) in imaging mode. DFOSC employs a 2k × 2k thinned Loral CCD, providing a $13.7' \times 13.7'$ FOV with a pixel scale of 0.″4/pixel (Andersen et al. 1995). Observations were taken using B, V, R and I filters, using non-sidereal tracking and multiple exposures of 60 seconds to minimize trailing effects, particularly during the first month after discovery when 3I/ATLAS appeared near the Galactic plane in the images.

2.3.6. GOTO

The Gravitational-wave Optical Transient Observer (GOTO) project is an array of wide-field optical telescope units located at both the Roque de los Muchachos Observatory on La Palma, and the Siding Spring observatory in Australia. GOTO detected 3I/ATLAS in eight difference images obtained over four nights between 2025 August 17 and 2025 August 23 using the Siding Spring node. Each telescope is equipped with a Finger Lakes Instrumentation ML50100 camera based on the KAF-50100 CCD sensor, which provides a pixel scale of 1.25″/pixel and a FOV of $2.1^\circ \times 2.8^\circ$. Although GOTO was not designed specifically for Solar System science, its large field of view enabled observations of 3I/ATLAS, which were obtained using the L-band, a broadband filter spanning the Sloan g', r', and Johnson V bands from 400–700 nm (Steeghs et al. 2022). All images had exposure times of 45 s, with the total number of

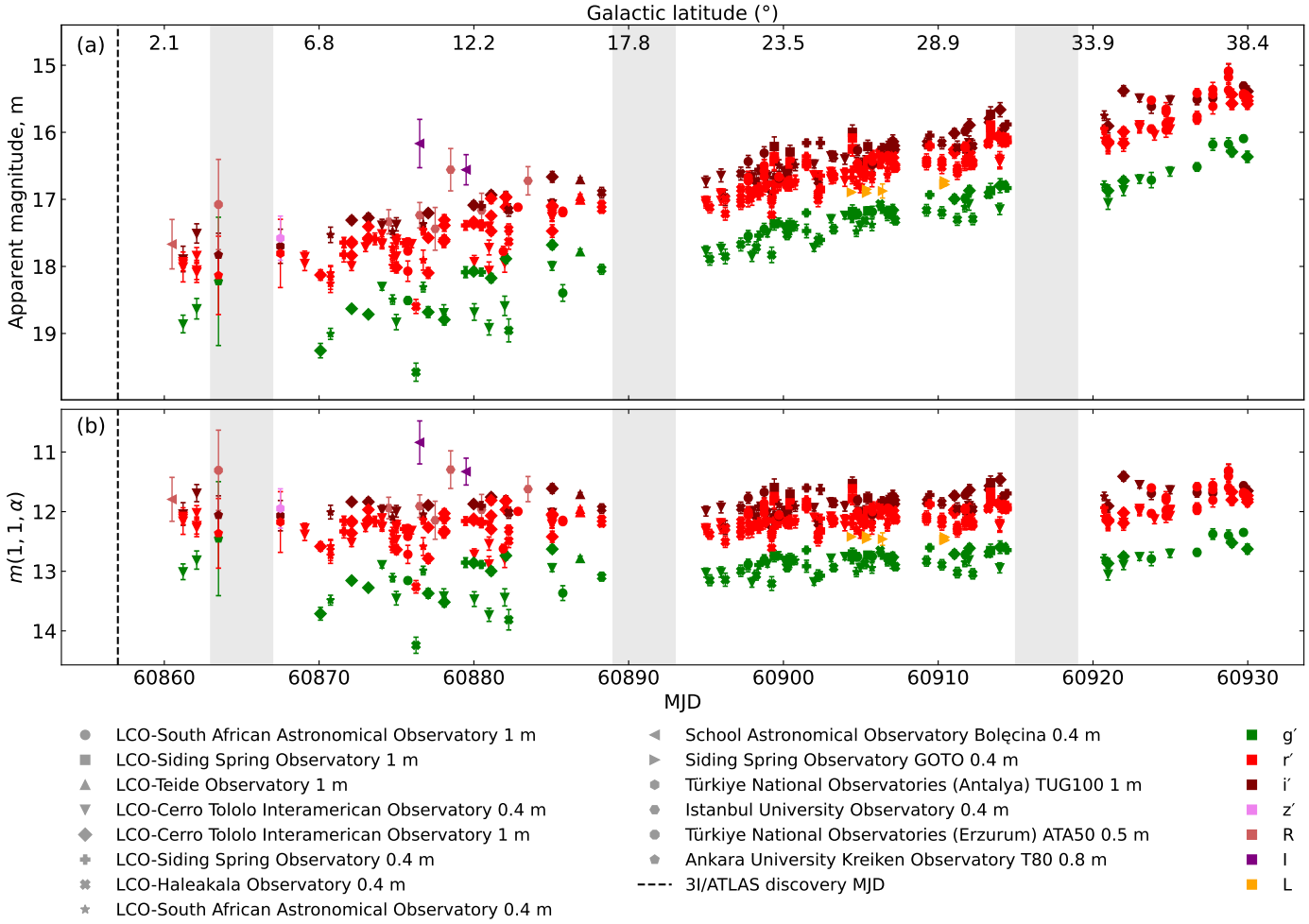


Fig. 2. Photometric evolution of 3I/ATLAS over the observing campaign. Apparent magnitude vs. MJD of interstellar comet 3I/ATLAS from PSF photometry is shown in the top panel a. The reduced magnitude, $m(1, 1, \alpha)$, is shown in the bottom panel b. The calibrated magnitudes are shown as a function of MJD, combining observations from multiple telescopes and filters. Marker shapes distinguish individual telescope datasets. g', r', and i' refer to the Sloan filter system; R and I refer to the J-C filter system; and L corresponds to the broad GOTO L-band. The vertical dashed line marks the discovery epoch, and the gray shaded regions indicate intervals when the Moon–comet elongation fell below 30°.

coadds varying between 2, 3, or 4 depending on the observation. Unlike the other observations presented in this study, the photometry of 3I/ATLAS from GOTO was not processed using the BHTOM pipeline. These data are nevertheless included for completeness, but were obtained using a different processing approach and may therefore exhibit systematic offsets relative to the other datasets used in this study. The AB magnitudes were calibrated against the ATLAS Refcat (Tonry et al. 2018a), and the L-band magnitudes were derived using differential photometry.

3. 3I/ATLAS measurements

3.1. The magnitude evolution of 3I/ATLAS

We measured the apparent magnitude of 3I/ATLAS as a function of Modified Julian Date (MJD) between UT 2025 July 04 and 2025 September 11, using BHTOM photometry calibrated to the GaiaSP system as described in Section 2.1. Figure 2a shows the resulting pre-perihelion light curve, spanning 70 days and combining observations from the facilities listed in Table A.1. The dataset comprises high-cadence photometry obtained in Sloan g', r' and i' bands, J-C R, and I bands, and the GOTO L-band, providing broad multiband coverage of the comet's magnitude evolution prior to perihelion. The D154T and UZO data were not included in this long-term light curve, as these observations were densely sampled over individual nights and their short-timescale structure would not be meaningfully represented in a 70-day light curve. They were instead considered separately in Section 4. To remove poor-quality measurements, we inspected images corresponding to data points that deviated significantly and unexpectedly from the temporal brightness trend. Sudden increases in brightness are plausible if the comet undergoes an outburst, but inspection showed that the outliers primarily resulted from poor image quality or, more commonly, contamination by nearby background sources where the comet signal became indistinguishable from a star. Such measurements were therefore excluded from the final light curve.

Although PSF photometry suppresses much of the dust-coma signal, it enables magnitude measurements in crowded fields, including the dense stellar regions near the Galactic plane where 3I/ATLAS was located around the time of discovery and during the first months of observations (July–August 2025). In Figure 2, we indicate the comet's Galactic latitude over the observing window (top axis), illustrating that 3I/ATLAS moved progressively away from the Galactic plane as the observing campaign progressed. This reduced contamination from nearby background

sources and helped to mitigate crowding-related systematics in the later measurements. This approach therefore still provides a useful estimate of the overall brightness and its evolution as the comet moved toward perihelion. Exposure times were selected such that the expected trailing of 3I/ATLAS was smaller than the seeing at the time of observation at each observatory site, minimizing any mismatch between the stellar PSF and the apparent profile of the comet. However, this approach likely introduced additional uncertainty, as the fraction of coma flux included in the PSF measurement may have varied with seeing conditions and the instrument PSF. In Section 5.2, we examine the dust properties of 3I/ATLAS using aperture photometry, which is more appropriate for measuring an extended coma.

Figure 2a shows that the magnitude of 3I/ATLAS brightened steadily over the 70-day observing window, with a total decrease of ∼3 magnitudes in each of the g', r', and i' bands. We found no evidence in the light curve for behavior that is inconsistent with the monotonic brightening that is typically observed for comets as the heliocentric distance decreases and the corresponding solar insolation increases. Inspecting the images individually, this brightening is consistent with the expansion of the dust coma and corresponding increase in flux. Martinez-Palomera et al. (2025) analyzed Transiting Exoplanet Survey Satellite (TESS) observations obtained between 2025 May 7 and 2025 June 2, spanning a ∼26-day window, and similarly reported a steady brightening with no evidence of anomalous behavior.

To investigate the extent to which the apparent brightening was influenced by the changing observing geometry, we also calculated the reduced magnitude, $m(1, 1, \alpha)$, for each filter, where α is the phase angle. This is the apparent magnitude the object would have at heliocentric and geocentric distances of 1 au, without applying a phase-angle correction. The reduced magnitude is given by

$$m(1, 1, \alpha) = m - 5 \log_{10}(R_h \Delta). \quad (1)$$

Here, m is the apparent magnitude in a given filter, and R_h and Δ are the heliocentric and geocentric distances, respectively. We obtained R_h and Δ for each observation using JPL Horizons (Giorgini et al. 1996). The reduced magnitudes are shown in Figure 2b. In comparison to the apparent magnitudes shown in Figure 2a, the reduced magnitudes show a much smaller overall change during the observing interval, indicating that a large fraction of the apparent brightening was caused by the changing observing geometry. However, we effectively could not detect the nucleus (because its photometric contribution would have been obscured by the shroud of activity) in these data, and these reduced PSF magnitudes therefore did not represent measurements of the nucleus. The PSF photometry sampled an approximately fixed angular aperture, such that the corresponding projected physical scale at the comet decreased as Δ also decreased. At the same time, the comet activity increased as R_h decreased. For a coma that behaves approximately as $1/\rho$, the enclosed flux scales with aperture radius, so the shrinking projected aperture could offset much of the intrinsic brightening of the coma, resulting in only a small change in the reduced magnitude. The reduced-magnitude evolution therefore provided a useful check on the role of geometry, but did not imply that the coma contribution within the PSF measurement was negligible or constant.

In Figures 2a, b, there are three multi-day gaps present in the dataset which are represented by gray shaded regions. These correspond to time periods where the Moon-comet elongation fell below 30°, during which observations from the LCOGT were temporarily suspended. We also note that most of the observations at MJD <60 890 (UT 2025 August 3) were obtained with smaller telescopes—primarily the LCOGT 0.4 m units—resulting in lower signal-to-noise ratios and correspondingly larger photometric uncertainties and overall scatter in the data. This was due to the comet brightness being close to the limiting magnitude of the 0.4 m telescopes and the crowded stellar fields.

3.2. The rotation period

The rotation period, $P_{\rm rot}$, of 3I/ATLAS was measured using multiband observations from LCOGT, UZO and the D154T. While the UZO and the D154T datasets provided dense intranight sampling, they were complementary to the longer-baseline LCOGT observations, which were taken several per night over 70 nights. The LCOGT data used in this section are the same measurements presented in the previous Section 3.1 of PSF photometry calibrated in the BHTOM using the Gaia XP low-resolution spectra. Inspection of the LCOGT light curve, discussed in Section 3.1, revealed a monotonic brightening, consistent with the gradual increase in coma size and overall cometary activity. When measuring the rotation period, and therefore focusing on the short-timescale variability associated with nucleus rotation, we de-trended the magnitudes in each of the filters used by the LCOGT by fitting and subtracting a linear function of time. This linear fit was not intended to represent a physical activity law, but was only used to remove the slow overall brightening over the observing window while preserving variability on hour timescales. The magnitudes measured from the UZO and the D154T datasets were not independently de-trended due to their short temporal baselines. To enable direct comparison between filters and datasets, we computed residual magnitudes by subtracting the mean magnitude of each filter from all measurements in that filter, removing constant offsets. These residuals were then used for the period search and, after a preferred period was identified, the combined residual light curve was phase folded to produce the final rotation light curve, as shown in the top panel of Figure 3.

A Lomb–Scargle (LS) periodogram (Lomb 1976; Scargle 1982) was computed using the detrended LCOGT residuals, which provided the longest temporal baseline, and the photometric uncertainties were used as the weights in the periodogram calculation. The UZO and D154T datasets were not included in the period search due to their shorter time coverage, which was insufficient to constrain rotation periods on hour timescales. Shown in the bottom panel of Figure 3, the resulting periodogram exhibited a dominant peak at a period of $P_{\rm LS}$ = 7.994 h, with a false-alarm probability (FAP; the probability that a peak of equal or greater power could arise from noise alone VanderPlas 2018) of < 1%, indicating this peak was unlikely to have arisen by chance. The width of the dominant peak, highlighted in gray, was used to estimate the uncertainty on the detected period, giving an uncertainty of ±0.038 h. We therefore report a best-fitting photometric periodicity of $P_{\rm LS}$ = 7.994 ± 0.038 h. As a check, we repeated the LS search using only the LCOGT r' data. This recovered the same dominant photometric periodicity, with $P_{{\rm LS},r'}$ = 7.9926 h and a FAP of < 1%. As an additional test, we split the LCOGT r' data into three observing intervals: MJD <60 890, 60 890 < MJD < 60 920, and MJD > 60 920. The ∼8 h signal was recovered clearly in the central interval, with a best-fitting period consistent with the full-dataset value of $P_{\rm LS}$ = 7.994 ± 0.038 h. The first and third intervals did not independently recover the same dominant

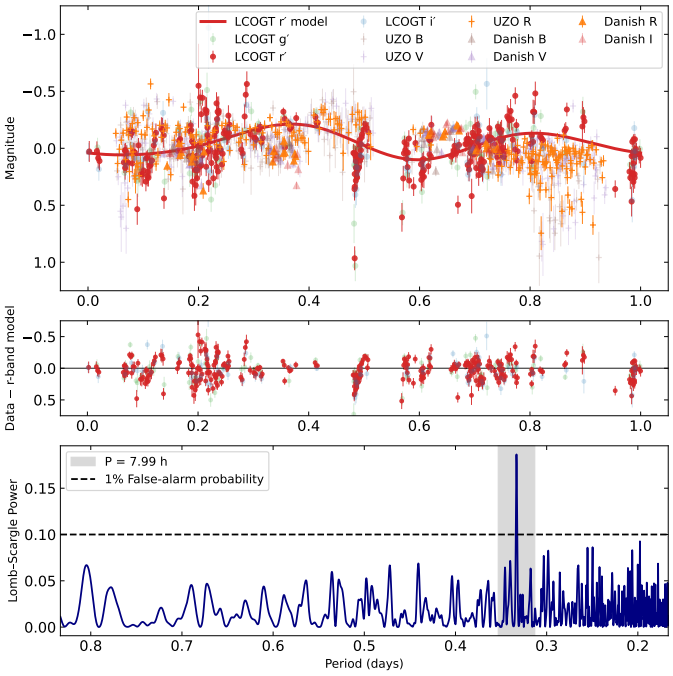


Fig. 3. Phase-folded rotational light curve and Lomb–Scargle periodogram of 3I/ATLAS. The top panel shows the phase-folded rotational light curve of 3I/ATLAS. Calibrated magnitudes were detrended for the long-term brightening and folded on the adopted rotation period of $P_{\rm rot}$ = 15.98 ± 0.08 h. LCOGT r', UZO R, and D154T R are shown in the foreground with the best-fitting three-harmonic sinusoidal model for the LCOGT r'-band overplotted. The background shows the entire remaining dataset from LCOGT g', i'; UZO B, V; and D154T B, V; and I. The middle panel shows the residuals of the LCOGT data relative to the LCOGT r' harmonic model. The bottom panel shows the LS periodogram of the detrended LCOGT residuals; the shaded region marks the strongest periodicity, and the dashed horizontal line indicates the 1% FAP level.

period. The quoted period therefore remains the value measured from the full LCOGT dataset, but the detection is mainly supported by the central interval.

Interpreting photometric periodicities in an active object was not straightforward as any nucleus-driven signal was likely obscured by the coma, and the light-curve shape could differ substantially from that of an inactive rotating body. In particular, the coma could have diluted or suppressed nucleus-driven light-curve variations due to the changing projected cross-section (Meech et al. 1993; Reyniers et al. 2009). The inner-coma dust brightness can also substantially vary over a single rotation as seen by in-situ measurements of 67P/Churyumov-Gerasimenko (Tubiana et al. 2019). Periodicities in the coma light curve may be expected if the dust originated from a localized active region on the nucleus, or from activity distributed globally over a non-spherical nucleus. In practice, both a single-peaked signal at $P_{\rm LS}$ and a double-peaked signal at $2P_{\rm LS}$ were plausible as shape-driven brightness variations can produce two similar maxima per full rotation (Kokotanekova et al. 2017). Serra-Ricart et al. (2026) also adopted a doubled-period under the assumption of a jet originating from a single active area near one of the rotational poles of the nucleus. We therefore also considered the doubled (alias) interpretation, under which the detected photometric periodicity would correspond to a possible nucleus rotation period of $P_{\rm rot} = 2P_{\rm LS}$ = 15.98 ± 0.08 h. However, the LS periodogram did not show an independent peak at $2P_{\rm LS}$, so the doubled value was not directly detected in the periodogram. We therefore treated $P_{\rm LS}$ as the measured photometric periodicity, while $2P_{\rm LS}$ remained a possible physical interpretation, and advise caution when trying to determine periodicity from any coma-obscured nucleus.

The phase-folded LCOGT g', r', and i' residual light curves were then fitted independently using a truncated Fourier series with three harmonics, consisting of a sum of sine and cosine terms plus a constant offset representing the mean residual magnitude in each band. Among the three bands, the r' data exhibited the highest signal-to-noise ratio and the lowest scatter, and were therefore adopted as the reference band. The best-fitting r'-band model was evaluated at the phases of all LCOGT, UZO, and D154T data points to determine whether the same phase-dependent behavior was present in the other datasets. The UZO and D154T R-band data are shown for comparison in the top panel of Figure 3.

The middle panel of Figure 3 shows the g', r', and i' residuals relative to their respective harmonic models, and does not show clear evidence of an additional periodicity beyond the adopted rotation signal. As a check, we compared the variance of the detrended LCOGT data before and after subtracting the fitted harmonic model in each band. The variance decreased by 11.5%, 19.3%, and 8.9% for the g', r', and i' data, respectively. We also tested the phase coherence of the folded light curve using the LCOGT r' data folded on $P_{\rm rot}$ = 15.98 h. The data were divided into 10 phase bins, and the within-bin variance was compared with 5000 randomized trials. The mean within-bin variance was 0.032 for the real data and 0.039 for the median of the randomized trials, and none of the randomized trials produced a lower mean within-bin variance than the real data. The maximum within-bin variance was 0.223 for the real data and 0.063 for the median of the randomized trials. We repeated the test using 6, 8, 10, 12, 15, and 20 phase bins, and in each case, the mean within-bin variance of the real data was lower than the median within-bin variance from the randomized trials, although the maximum within-bin variance depended on the number of phase bins. Repeating these tests with the UZO R and D154T R data included did not improve the variance or phase-dispersion results. We therefore retained the LCOGT data as the primary period-search dataset and treated the UZO/D154T data as a consistency check. The best-fitting LCOGT r' model had an amplitude of 0.16 mag; however, the inherent amplitude can be diluted by seeing-dependent variations in the inner-coma photometry (Licandro et al. 2000), and the aperture crossing timescales of the expanding dust coma. We therefore did not interpret the measured amplitude in terms of nucleus elongation. The standard deviation of the model-subtracted residuals was σ = 0.19 mag.

de la Fuente Marcos et al. (2025) found a rotation period of $P_{\rm rot}$ = 16.79 ± 0.23 h using a folded light curve from data taken using the Two-meter Twin Telescope (TTT) on July 2, July 3 and July 5. (Santana-Ros et al. 2025) found a similar rotation period of $P_{\rm rot}$ = 16.16 ± 0.01 h using photometric data from multiple telescopes including Telescopi Joan Oró, The Faulkes Telescope South, The Faulkes Telescope North, The Lesedi telescope, and the Nordic Optical Telescope from July 2 to July 29. A month later, in August 2025, Serra-Ricart et al. (2026) used multiple-night imaging from the *TTT* at the Teide Observatory in the Canary Islands (Spain) to study a faint high-latitude jet in the inner coma. From the jet morphology analysis, the authors determined a rotation period of $P_{\rm rot}$ = 15.48 ± 0.70 h, a month after the two aforementioned studies. The authors attribute this discrepancy to either the intrinsic uncertainties in their

methodology or to 3I/ATLAS changing its rotation period due to the outgassing torques. Adopting our doubled-period solution of $P_{\rm rot}$ = 15.98 ± 0.08 h, our measurement was consistent with the value reported by Serra-Ricart et al. (2026) within 1σ, and consistent with the period reported by Santana-Ros et al. (2025) at the ∼2σ level. The slightly longer period measured by de la Fuente Marcos et al. (2025) differed at the ∼3σ level, although there is no requirement that the rotation period is constant with time. We also blindly phased the LCOGT r' data using the published rotation periods and repeated the same phase-dispersion test. The mean within-bin variance was 0.038 for $P_{\rm rot}$ = 16.79 h (de la Fuente Marcos et al. 2025), 0.038 for $P_{\rm rot}$ = 16.16 h (Santana-Ros et al. 2025), and 0.039 for $P_{\rm rot}$ = 15.48 h (Serra-Ricart et al. 2026), compared with 0.032 for $P_{\rm rot}$ = 15.98 h from this work. The adopted doubled-period interpretation therefore gives the lowest phase dispersion in our data, while the literature periods remain broadly comparable. We therefore regard our result as consistent with the range of published values, but not as a unique determination of the physical rotation period. Overall, the published rotation periods for 3I/ATLAS span 15.48–16.79 h, and our measured value of $P_{\rm rot}$ = 15.98 ± 0.08 h is consistent with this range. As discussed above, the LS periodogram directly detected a photometric periodicity of $P_{\rm LS}$ = 7.994 ± 0.038 h, while $P_{\rm rot}$ = 15.98 ± 0.08 h remained a possible doubled physical interpretation. The rotation period should therefore be interpreted with caution.

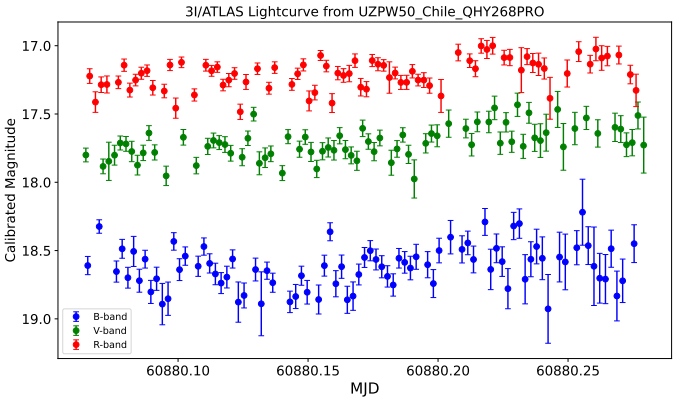
4. High-cadence observations and colors

4.1. High-cadence observations

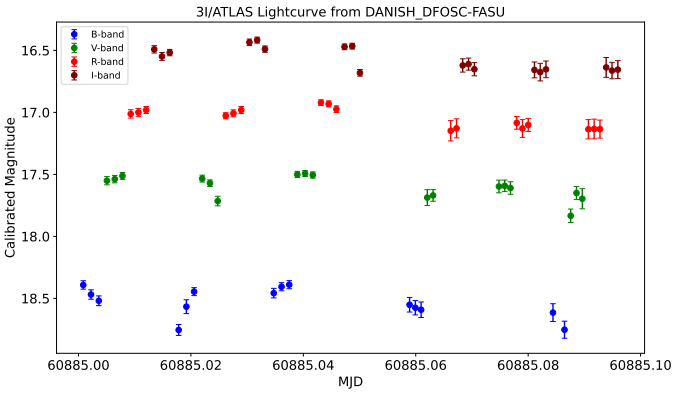
Complementary to the nightly monitoring of 3I/ATLAS described in the previous sections, we obtained high-cadence intra-night imaging from two facilities: the 0.5 m UZO telescope and the D154T. These observations are densely sampled over individual nights and are therefore not included in the long-term light curve shown in Figure 2, which is intended to illustrate the overall magnitude evolution over the 70-day observing interval. The UZO dataset comprises 656 J–C B, V and R observations obtained over five nights between UT 2025 July 17 and 2025 July 24 (MJD 60 873–60 880). The D154T observations were obtained over three nights at La Silla and provide densely sampled light curves in the J–C B, V, R, and I bands. Both the UZO and the D154T datasets were calibrated via the BHTOM processing pipeline using the PSF photometry method. Representative single-night light curves from each facility are shown in Figure 4 and the full set is presented in Appendices B and C, respectively. We used the densely sampled data to perform the color analysis shown in Section 4.2.

4.2. Color analysis

In both Figures 4a and 4b, there is minimal magnitude variation (less than 0.1 magnitude at most) across the J-C B, V, R and I bands, consistent with previous studies (Kareta et al. 2025; Seligman et al. 2025). There is a wealth of color data across multiple epochs. Thus we averaged the measured calibrated magnitudes for each filter taken on the same night for each dataset. The time span of these averages was typically several hours, roughly a quarter of the ∼8 h single-peaked period, over which rotational variability up to the light-curve half-amplitude (∼0.2 mag) would be expected. Next the D154T and UZO $BVRI$ magnitudes were converted to Sloan g', r', and i' magnitudes using the transformations given in Lupton (2005).



(a)



(b)

Fig. 4. Representative high-cadence intra-night photometry of 3I/ATLAS. (a) UZO observations on MJD 60 880 over 4.8 hours. (b) D154T observations on MJD 60 885 over 1.2 hours. The blue, green, red, and maroon points represent the J-C B, V, R, and I bands, respectively. The remaining high-cadence light curves are shown in the Appendices B and C.

The normalized spectral reflectivity and associated uncertainty in each filter was then calculated relative to the g' filter using the following equations:

$$R_\lambda = \frac{10^{-0.4[m_\lambda - m_\lambda(\odot)]}}{10^{-0.4[m_g - m_g(\odot)]}}, \tag{2}$$

$$\sigma_{R_\lambda} = 0.92103\, R_\lambda \left[\sigma_\lambda^2 + \sigma_g^2 + \sigma_\lambda(\odot)^2 + \sigma_g(\odot)^2\right]^{0.5}. \tag{3}$$

In these relationships, m_λ is the magnitude in the bandpass, σ_λ is the uncertainty on m_λ, σ_r is the uncertainty on m_r, and $m_\lambda(\odot)$ is the absolute magnitude of the Sun in that bandpass with uncertainty $\sigma_\lambda(\odot)$. We use $m_g(\odot) = 5.12 \pm 0.02$, $m_r(\odot) = 4.69 \pm 0.03$, $m_i(\odot) = 4.57 \pm 0.03$, and $m_z(\odot) = 4.60 \pm 0.03$ (Karaali et al. 2005; Rodgers et al. 2006).

Each observation's spectral reflectivity across the g', r', and i' filters is shown in Figure 5a, as well as their corresponding g-r and r-i values in Figure 5b, and are color coded by their heliocentric distance. The reddest reflectivities of 3I/ATLAS are observed when the comet is further from the Sun in its orbit, and the bluer reflectivities are highly centralized when the object is nearing 2 au.

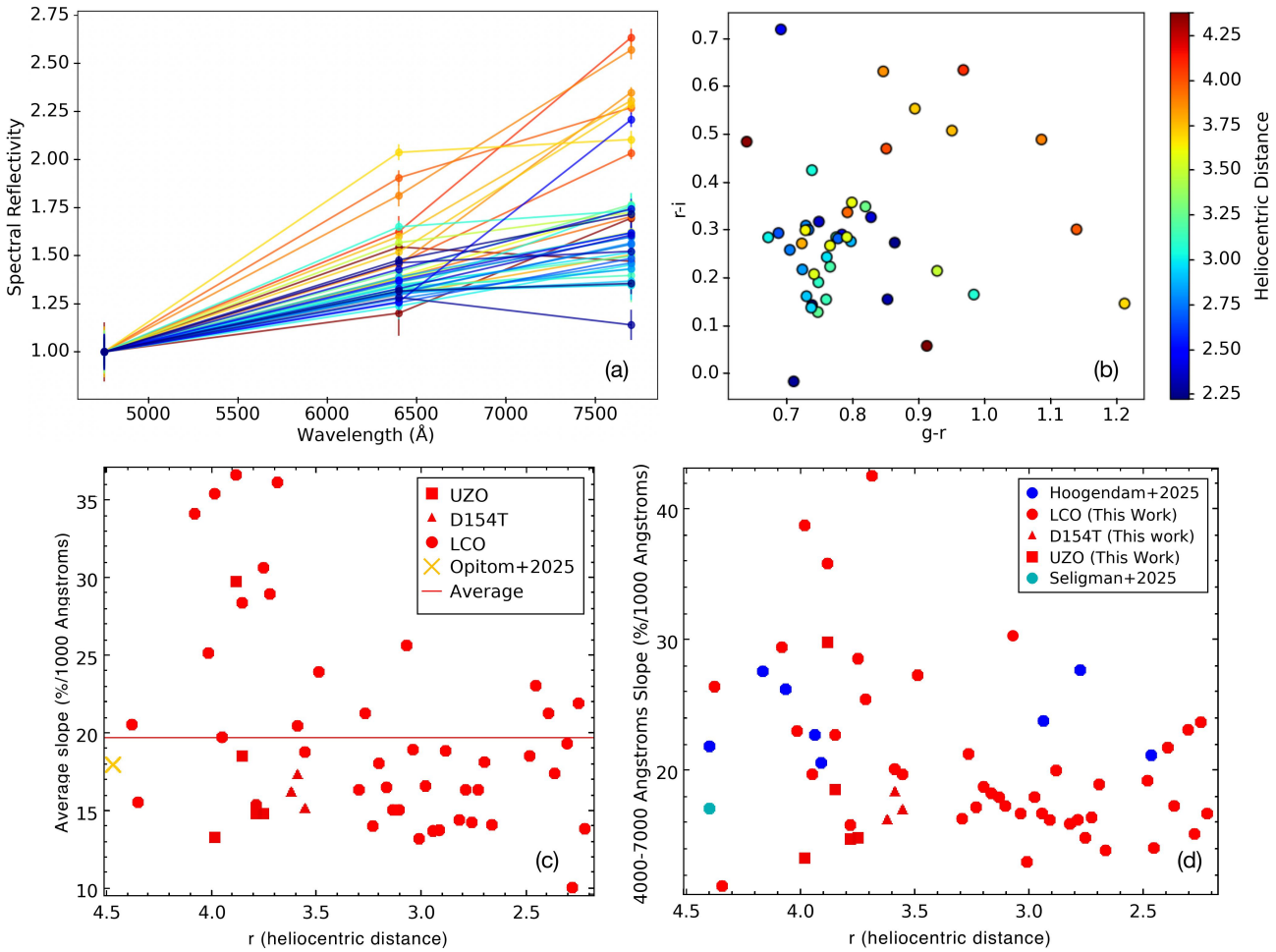


Fig. 5. Color measurements of 3I/ATLAS from the LCOGT, UZO, and Danish 1.54 m datasets. Panels a and b show the normalized spectral reflectivity for each observing night as a function of wavelength, and the corresponding g–r vs r–i distribution, respectively, color coded by heliocentric distance. Panel c shows the reflectivity slope averaged across 4000–8500 Å and normalized to the V filter as a function of pre-perihelion heliocentric distance. The yellow cross shows the value reported by Opitom et al. (2025), and the horizontal red line shows the average slope from our data. Panel d shows the spectral slope between 4000–7000 Å in comparison to the Hoogendam et al. (2026) slopes across the same wavelength range.

The spectral slope, S, between two filters, normalized at filter g, was calculated with the following relation:

$$S_g = \frac{10^5}{\lambda - \lambda_g}(-1 + 10^{-0.4((m_\lambda - m_g) - (m_\lambda(\odot) - m_g(\odot)))}), \quad (4)$$

where λ is in units of Å, and S is in units of $\%/10^3$ Å. We determine the spectral slopes normalized to the g filter for both the r and i filters, and then compute the average spectral slope for each observation date. We compared this approach to the traditional method of calculating the spectral slope by fitting a line to the normalized reflectivity. Both methods produce comparable results within $1\%/10^3$ Å. This average spectral slope spans 4000–8500 Å. We also calculated the spectral slope independently across the g and r filters (4000–7000 Å) to allow direct comparison to literature values across the same wavelength range. Finally, we changed our normalized filter to V (5500 Å) using the following relation:

$$S_V = \frac{S_g}{1 + \frac{\lambda_V - \lambda_g}{10^5} S_g}. \quad (5)$$

The average spectral slopes spanning 4000–8500 Å and 4000–7000 Å are shown as a function of pre-perihelion heliocentric distance in Figures 5c and 5d, respectively. This allowed for direct inspection of the general trend of color changes across the orbit of 3I/ATLAS. For data taken when 3I/ATLAS was between 4.47 au and 3.5 au, we found a large scatter in colors, with a tendency towards redder colors quantified by the large scatter in spectral slopes, and evident in the LCO light curve before UT 2025 August 3 (MJD 60 890) in Figure 2. As stated previously, this is likely due to the variability of photometry caused by the target being near the galactic center and in a densely crowded field.

The spectral slope of the normalized reflectivity measured by Opitom et al. (2025), when the object was at 4.47 au, is displayed for comparison in Figure 5c by an orange cross. As this is a more robust measurement of the reflectivity than photometry, it is a reasonable assumption that the photometric colors for heliocentric distances larger than 3.5 au lie closer to this data point. Neglecting the high spectral slopes measured before 3.5 au, there may be a weaker negative trend present indicating that 3I/ATLAS is getting bluer as it approaches perihelion;

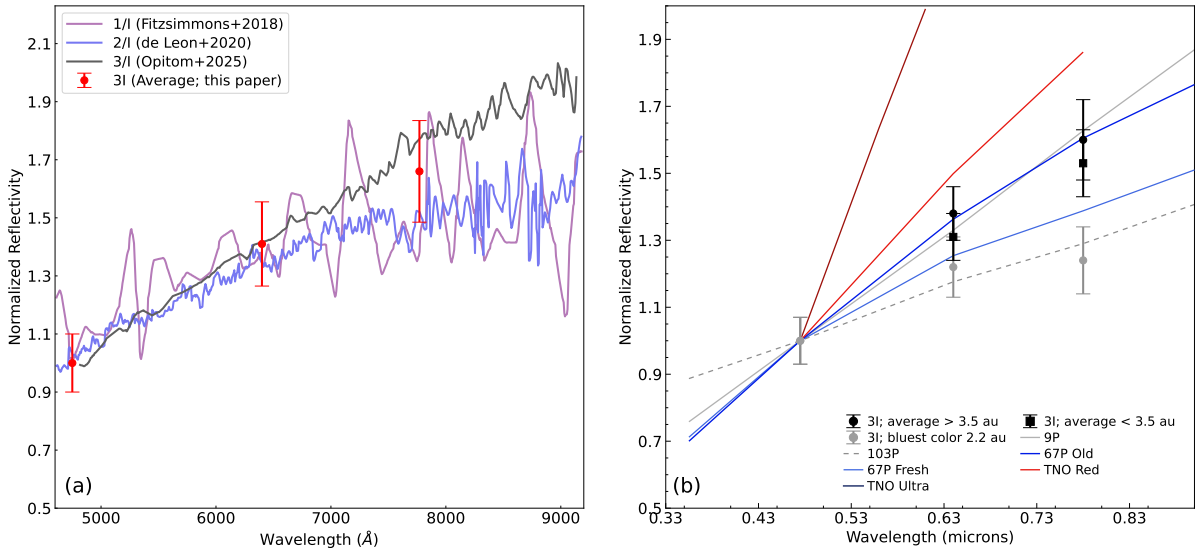


Fig. 6. Normalized reflectivity measurements of 3I/ATLAS derived in this work and their comparison with previous observations and representative small Solar System bodies. Panel a: average normalized reflectivity measured in this work together with literature spectra from Fitzsimmons et al. (2018), de León et al. (2020), and Opitom et al. (2025). Panel b: average reflectivity of 3I/ATLAS at $r_h > 3.5$ au and $r_h < 3.5$ au together with the bluest measurement at $r_h \sim 2.2$ au compared to representative normalised reflectivity trends from other small Solar System bodies, including TNOs (Delsanti et al. 2004), 9P/Tempel 1 (Li et al. 2007), 67P/Churyumov-Gerasimenko (Fornasier et al. 2016), and 103P/Hartley 2 (Li et al. 2013).

however this is not statistically significant. Taking the average of all spectral slopes from the entire duration of the pre-perihelion data, it is in agreement within 1 sigma with the spectral slope measured by (Opitom et al. 2025) shown in Figure 6a. We also show the spectral slopes across 4000–7000 Å to compare to literature values in Figure 5d. Both Seligman et al. (2025) and Hoogendam et al. (2026) cite spectral slopes that are statistically in agreement with our measured values.

The minor change in average slope between pre- and post-3.5 au and corresponding reflectivities is shown in comparison to other Solar System small bodies in Figure 6b with black circles and squares, respectively. The maximum color difference for 3I/ATLAS, at $R_h < 3$ au, is also shown for comparison in Figure 6b in gray circles. If one interprets the colors as non-changing, the spectral slope of 3I/ATLAS is comparable to other Jupiter-family comets such as 9P/Tempel 1 (Li et al. 2007; Kolokolova et al. 2016; Kelley et al. 2017) and even red trans-Neptunian objects (TNOs; Delsanti et al. 2004). If there is a real color change, it may be explained by the growing development of activity, which has been seen by previous studies to have an effect on an object's color. For example, objects that become bluer may be due to ice deposits revealed on the surface, or due to gas contamination, especially in the bluer filters (Meech et al. 2017a; Fornasier et al. 2016; Bufanda et al. 2023). If the object becomes redder, this could be due to larger dust grains that have physically fallen back onto the surface of the comet (Bufanda et al. 2023). The maximum possible change in spectral slope, shown in Figure 6b by the difference between black and gray data points, would be similar to the color change observed on 67P/Churyumov-Gerasimenko which is shown in Figure 6b by the blue and light blue trends, after activity revealed fresh ice on the surface of the comet (Fornasier et al. 2016). This is unlikely, however. This is an upper limit on the color change; it is therefore less likely that the effect would be this pronounced as the coma of 3I/ATLAS was still developing. Future studies need to be performed to validate any change in spectral slope, in particular, the most robust studies will come from follow-up spectroscopy near and after perihelion.

Table 1. Observations used in aperture photometry between UT 2025 August 10 and 2025 September 11 (MJD 60 897 and MJD 60 929).

Observatory	No. of observations
LCOGT-CTIO	40
LCOGT Siding Spring Observatory	12
LCOGT-SAAO	31

Notes. All telescopes used in aperture photometry were the LCOGT 1 m telescopes.

5. Cometary dust activity

5.1. Observations, aperture photometry, and calibration

In the previous sections, we analyzed the evolving magnitude of 3I/ATLAS using PSF photometry calibrated with the BHTOM pipeline. For the analysis of cometary dust activity, however, aperture photometry is more appropriate, as it captures flux from the extended coma rather than assuming a point source, an assumption that does not hold for active comets such as 3I/ATLAS. For optimal aperture photometry, we aimed to minimize the contamination from background sources and avoid over-subtraction of the sky background, and therefore we included only images taken when 3I/ATLAS was located in relatively uncrowded stellar fields (Kalberla & Kerp 2009). This was away from the Galactic plane at MJD > 60 897 (UT 2025 August 10) at a Galactic latitude of 22°. Using these data, we measured the apparent magnitude of 3I/ATLAS as a function of time. In total, 83 r'-band images obtained with the LCOGT 1 m telescopes were used in the aperture photometry analysis as shown in Table 1 which provided the highest signal-to-noise ratios and a sufficiently long baseline.

The position of 3I/ATLAS in each image was determined by the predicted positions obtained from ephemerides generated using JPL Horizons (Giorgini et al. 1996). For each image,

the predicted sky position at the time of observation was converted to detector coordinates using the image WCS, and the exact center of 3I/ATLAS was further refined via centroiding in order to ensure accurate aperture placement. The centroid refinement applied pixel-coordinate corrections relative to the ephemeris-predicted location of order $\Delta x, \Delta y \sim (0.4–3.9)$ pixels, corresponding to ∼0.3″–2.9″. The centroid was measured by fitting a two-dimensional Gaussian profile around the predicted position using the *Photutils centroid_2dg*[3] routine. To measure the local sky background around the comet, we measured the flux within a circular sky annulus at 5×10^4 km from the comet. This distance was selected in order to be sufficiently close to the comet where the sky was representative of the flux within the aperture, but far away enough that we avoided any coma contamination within the annulus during sky subtraction. A fixed circular aperture corresponding to a radius of 10 000 km at the comet was adopted for all images. This radius is typically employed for active comets (Snodgrass et al. 2013; Gardener et al. 2022; Gillan et al. 2024, 2025; Bolin et al. 2025; Chandler et al. 2026) in order to ensure changes in the measured flux reflect the intrinsic evolution of 3I/ATLAS within a constant physical aperture, while also facilitating direct comparison with other studies.

Stellar centroids were measured, and instrumental magnitudes were derived using circular apertures with radii defined relative to each measured stellar FWHM, with local sky backgrounds estimated from the surrounding annuli. Stars with poorly defined or non-stellar radial profiles, including saturated sources and objects affected by blending or edge effects, were excluded from the calibration sample. This ensured that only well-behaved stellar profiles were used to determine the photometric solution. Standard aperture corrections and zero-point corrections were then applied to the instrumental magnitudes. Photometric calibration was performed independently for each image using field stars returned from the *Gaia Data Release 3* catalog (Gaia Collaboration 2016, 2023 b) via the *Astroquery* (Ginsburg et al. 2019) *cone_search* routine centered on the location of 3I/ATLAS. We searched within a 290″ radius. The Gaia G-band (350–1050 nm; Weiler 2018) is an unfiltered wide band (white) and the integrated flux of the low-resolution blue photometer (BP) and red photometer (RP) spectra give G_{BP} and G_{RP} magnitudes from 350–680 nm and 630–1050 nm respectively (Jordi et al. 2010; Weiler 2018). Gaia G-band magnitudes and $(BP - RP)$ colors from the catalog were converted to Sloan g' and r' magnitudes using published color transformations[4] to give the calibrated r'-band magnitudes that were used. For the color-term correction to the comet magnitude, we assumed $(g' - r')_{\rm SDSS} = 0.57 \pm 0.05$, consistent with typical active-comet colors from Solontoi et al. (2012). We note that the Gaia-to-Sloan transformations are approximate and do not explicitly account for possible gas emission features in cometary spectra, including those of 3I/ATLAS.

When the calibrated magnitudes were calculated, we manually inspected each outlying measurement from the resulting light curve. We rejected any magnitude measurements of 3I/ATLAS that were affected by thick cloud cover where the data were unusable, had poor image quality, close proximity to a nearby bright object resulting in significant flux contamination within the aperture, or cases where the comet lay too close to the edge of the frame which prevented a reliable background measurement. The resulting apparent magnitude of 3I/ATLAS, measured within a 10 000 km radius aperture, as a function of time is shown in the top panel of Figure 7.

5.2. The dust production rate

In order to quantify the relative dust activity from 3I/ATLAS, we used the $Af\rho$ parameter which is commonly used as a proxy for the dust production rate in comets (A'Hearn et al. 1984). $Af\rho$ was measured from the calibrated aperture magnitudes using Equation (6) and is typically measured in centimeters.

$$Af\rho = \frac{4R_h^2\Delta^2}{\rho} \cdot 10^{0.4(m_\odot - m_c)} \tag{6}$$

Here, $m_\odot$ and m_c are the magnitude of the Sun and 3I/ATLAS, respectively, in the same filter. R_h is the heliocentric distance in au, Δ is the geocentric distance measured in cm, which returns $Af\rho$ in units of cm. The radius of the photometric aperture on the sky at the comet is given by ρ. Finally, we converted all of our $Af\rho$ measurements to a common phase angle of $\alpha = 0°$ using the Schleicher-Marcus phase function (Schleicher 2010) to give $A(0°)f\rho$. The corresponding evolution of $A(0°)f\rho$ vs MJD in the 1 m LCOGT r'-band images is shown in the middle panel of Figure 7. Visual inspection of the images used in the aperture photometry clearly revealed the presence of a surrounding dust coma. Formally, $Af\rho$ is most directly interpretable under the assumption of a steady-state coma, and could be affected by anisotropic emission (e.g., jets) or grain evolution within the coma. Our visual inspection of the frames did not reveal any obvious prominent jets, spirals, or other strong morphological features. Over this time period, from UT 2025 August 10 to 2025 September 11 (MJD 60 897 to MJD 60 929), we measured an increase in $A(0°)f\rho$ from ∼600 cm to 1100 cm as the comet approached the Sun from a heliocentric distance of 3.18 au to 2.19 au. This range of $Af\rho$ measurements is consistent with other recent studies of 3I/ATLAS (Scarmato 2025) at similar heliocentric distances.

Comparing the dust production rate of 3I/ATLAS to other dynamical populations in the Solar System, the dust activity is higher than what is typically observed for most JFCs at comparable heliocentric distances (Gillan et al. 2024, 2025). However, some similar activity levels have been reported for some of the more active JFCs, such as 19P/Borrelly (Fink 2009) and 67P/Churyumov–Gerasimenko (Snodgrass et al. 2013, 2017; Gardener et al. 2022; Gillan et al. 2025; Rosenbush et al. 2026), particularly near perihelion. In addition, 3I/ATLAS exhibits a significantly higher dust activity than the previously discovered interstellar comet 2I/Borisov (Fitzsimmons et al. 2019; Jewitt & Luu 2019), while showing activity levels more comparable to those measured for some long-period comets at similar heliocentric distances (Mazzotta Epifani et al. 2014; Garcia & Gil-Hutton 2021).

5.3. The mass-loss rate

From $A(0°)f\rho$, an approximate dust mass-loss rate, Q_d, in kg s^{-1} can be inferred. Under simplified assumptions for the dust grain radius, ejection velocity, and grain density, we calculated an order-of-magnitude estimate of the particulate mass loss

[3] https://photutils.readthedocs.io/en/stable/api/photutils.centroids.centroid_2dg.html
[4] https://gea.esac.esa.int/archive/documentation/GDR3/Data_processing/chap_cu5pho/cu5pho_sec_photSystem/cu5pho_ssec_photRelations.html

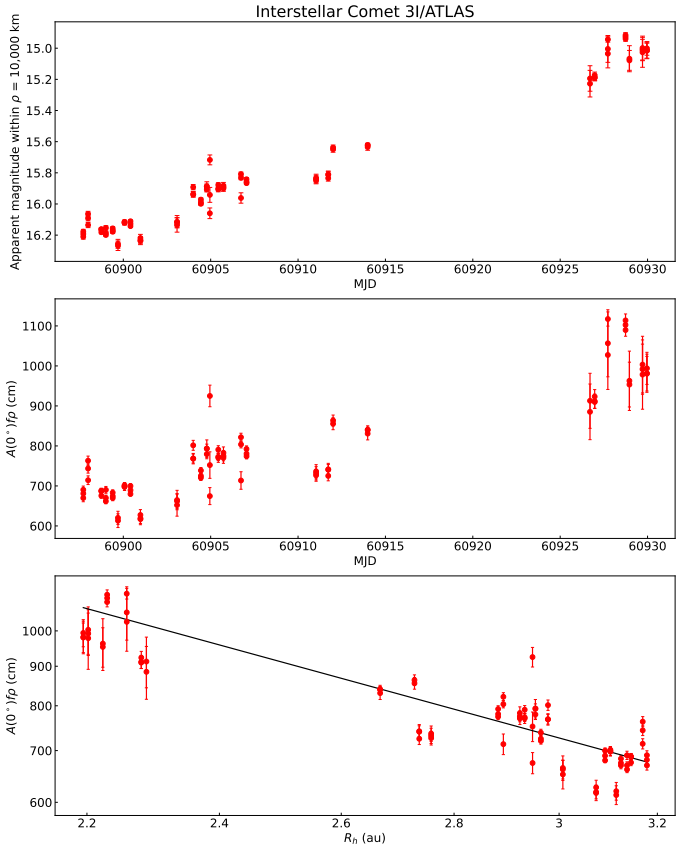


Fig. 7. Dust production and activity evolution of 3I/ATLAS. Top panel: aperture photometry light curve of 3I/ATLAS. Middle panel: dust production parameter $A(0°)f\rho$ vs. time in MJD. Lower panel: $A(0°)f\rho$ vs. heliocentric distance with the solid line representing the $A(0°)f\rho$ activity index, n. The red markers on the plots represent the 1 m LCOGT r'-band measurements.

from 3I/ATLAS over the observing period (Fink & Rubin 2012; Ivanova et al. 2018). However, such calculations are inherently speculative and highly sensitive to the adopted grain properties, with the inferred mass-loss rate possibly varying by at least an order of magnitude (Gillan et al. 2025). These assumptions are also expected to vary with heliocentric distance. We therefore calculated Q_d solely to gauge the physical mass loss from the nucleus and emphasize that the resulting values should be regarded as approximate, order-of-magnitude estimates. The relationship between $Af\rho$ and the dust mass-loss rate is given in Equation (7) by

$$Q_d = Af\rho \frac{4\pi r_d \sigma_d v_d}{3 p_r}, \tag{7}$$

where r_d is the dust grain radius, σ_d is the grain density, v_d is the dust ejection velocity, and p_r is the geometric albedo in the Sloan r'-band. In this work, fixed dust properties were adopted; a more accurate approach would require a grain size and density distribution. Following the large-grain, low-velocity scenario proposed by Jewitt & Luu (2025b), we assumed r_d = 100 µm and v_d = 5 m s^{-1}. We further adopted a typical cometary albedo of p_r = 0.04 and a grain density of 1 g cm^{-3}. To obtain the range of mass loss rates, we took the minimum $A(0°)f\rho = 665 \pm 24$ cm on 2025 August 16 at 3.18 au and a maximum $A(0°)f\rho = 994 \pm 40$ cm on 2025 September 11 at 2.19 au and converted these to Q_d. We measured an increase in the dust mass-loss rate from ≤217 kg s^{-1} to ≤328 kg s^{-1} over the ∼1 month observing period using the 1 m r'-band LCOGT data. These values represent upper limits and are comparable to mass-loss rates reported in other studies of 3I/ATLAS. Chandler et al. (2026) reported dust mass-loss rates of ∼10–100 kg s^{-1}, depending on the assumed grain radius (1–10 µm), while Bolin et al. (2025) predicted a lower value of ∼0.1–1 kg s^{-1} using early, preliminary data that have since been refined. The higher mass-loss rates measured in this work are likely caused by the smaller heliocentric distance during our observations. Both comparison studies were conducted within approximately one week of discovery, where lower dust production is typically expected further from the Sun. We reiterate that all dust mass-loss estimates are highly sensitive to the underlying assumptions regarding grain properties, both here and in the comparison studies.

5.4. The activity index

We measured the activity index, n, defined as the power-law exponent of how $A(0°)f\rho$ varies as a function of heliocentric distance, R_h, such that

$$A(0°)f\rho \propto (R_h)^n. \tag{8}$$

The activity index was determined by fitting a power-law relation to the $A(0°)f\rho$ measurements as a function of heliocentric distance, shown in the bottom panel of Figure 7. The fit was performed in log–log space using a weighted least-squares approach, with the propagated uncertainties on $A(0°)f\rho$ used as weights. We measured an activity index of $n = -1.24 \pm 0.02$. Activity driven solely by gas sublimation, in the limiting approximation where all of the absorbed solar energy goes into sublimation, would result in an activity index of approximately $n = -2$, due to the absorbed solar energy decreasing as the inverse square of heliocentric distance. The shallower slope we have measured therefore indicates that the dust activity of 3I/ATLAS does not scale directly with sublimation alone. Instead, n is consistent with the presence of an already well-developed dust coma that evolves more gradually with decreasing heliocentric distance, rather than reflecting a sharp turn-on of activity or outbursts. This interpretation is supported by the detection of a dust coma from the time of discovery (Seligman et al. 2025; Chandler et al. 2026), and that it has also been active since pre-discovery at 6.5 au (Ye et al. 2025). In addition, the shallower slope may be influenced by the dominance of relatively slow-moving, larger dust grains (Jewitt & Luu 2025b), that take longer to accelerate and remain within the aperture for longer timescales. We also note that the activity index derived here is based on observations spanning a relatively narrow heliocentric distance range and may therefore not be representative of the comet's long-term activity behavior. The activity index derived here is shallower than values reported in brightness-based studies of 3I/ATLAS. Jewitt & Luu (2025b) measured an activity index of $n = -3.8 \pm 0.3$ from heliocentric brightness variations over a distance range of 4.6–1.8 au, while a similar brightening rate was reported in Ye et al. (2025). For comparison with $A(0°)f\rho$, Jewitt & Luu (2025b) also used a fixed physical aperture of 10 000 km, and removing the r_h^{-2} dependence from incident sunlight gives an equivalent dust-activity scaling of approximately $n = -1.8$. This is somewhat steeper than, but consistent within 2σ with the value of $n = -1.24 \pm 0.02$ measured here, given the different heliocentric distance ranges.

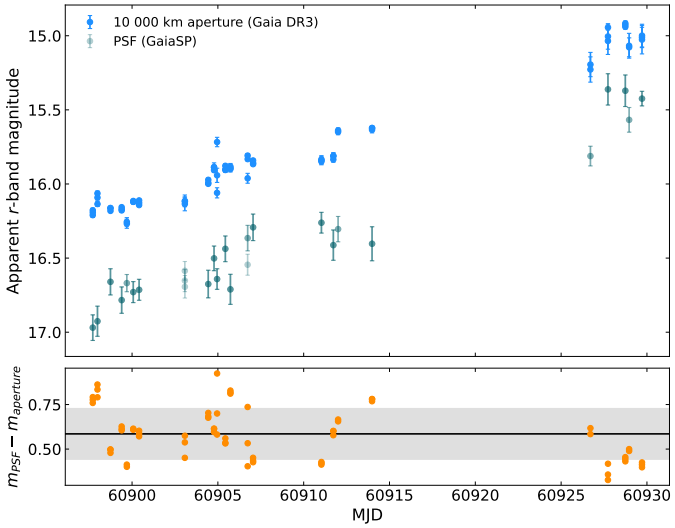


Fig. 8. Comparison of PSF and fixed-aperture photometry of 3I/ATLAS. Upper panel: comparison between the PSF photometry (teal) and the fixed-aperture photometry (blue) using the LCOGT 1 m r'-band images. Lower panel: magnitude difference $m_{PSF} - m_{aperture}$ (orange) for the measurements matched in MJD, with the gray shaded region indicating the 1σ scatter from the median offset.

6. Discussion

6.1. PSF and aperture photometry

We used two independent photometric pipelines for the image processing. PSF photometry was performed using the BHTOM pipeline, calibrated to the GaiaSP catalog as described in Section 2.1, while the fixed-aperture photometry was calibrated against the Gaia-DR3 catalog magnitudes (Gaia G, BP, RP). As magnitude measurements from both calibration methods were available in the LCOGT 1 m r'-band data, they were compared to assess the contribution of the extended dust coma for an active comet.

During the aperture photometry analysis, measurements affected by poor image quality or aperture flux contamination were rejected as described in Section 5.1. As this filtering was applied specifically to the aperture photometry, not every aperture measurement had a corresponding PSF measurement obtained at the same epoch. For the comparison shown in Figure 8, PSF and aperture photometry were compared on a per-image basis, and only measurements from the same exposure were included; where an exact one-to-one match was not available due to filtering, the nearest-time PSF measurement was used. The comparison is a subset of 68 matched measurements, drawn from the 83 aperture photometry points shown in Figure 7. For clarity, the PSF photometry measurements in Figure 8 are plotted with reduced opacity. The PSF photometry exhibits significantly less scatter than the fixed-aperture measurements in this dataset. However, PSF photometry can be more dependent on image conditions, since a larger PSF core can include more coma flux in the PSF fit. Aperture photometry, if the aperture is large with respect to the PSF width, should be less affected by seeing, but is more sensitive to the accuracy of the background removal, nearby stars, and residual aperture contamination. The two light curves in Figure 8 show the same temporal behavior but are offset by a nearly constant amount. Overall, the PSF photometry is fainter than the aperture photometry measurements, which should be expected since the aperture photometry also includes the flux from the extended dust coma. The median magnitude offset is 0.59 magnitudes which corresponds to a factor of ∼1.7 difference in flux. This implies that the flux measured within the fixed aperture is approximately 1.7× that which was measured using PSF photometry. This was consistent with an additional contribution from extended dust emission within the aperture. For this dataset, this corresponded to roughly 40–45% of the optical flux within the aperture arising from extended dust emission rather than the pseudo-nucleus. However, because the angular size of the 10 000 km aperture changed with Δ, while the PSF scale was set by the seeing, this fraction depended on the observing geometry and should therefore be interpreted only in the context of the matched measurements shown here.

6.2. Implications for BHTOM in time-domain monitoring of small bodies

The observations of 3I/ATLAS presented in this work provide a practical demonstration of coordinated, long-baseline monitoring of an active interstellar comet. The 70-day coverage, obtained using a geographically distributed network of facilities, enabled the evolution of the comet's magnitude and dust activity to be characterized independently of short-timescale variability and survey cadence effects. Such extended, high-cadence monitoring is particularly valuable for ISOs, which can evolve rapidly during the limited intervals over which they are observable from the ground where they can become unobservable due to a lack of activity or solar elongation constraints. In this case, the sustained coverage allowed the gradual brightening and dust production of 3I/ATLAS to be observed continuously, while also supporting the interpretation of the rotational and activity-related behavior. 3I/ATLAS was not a trivial test case for applying BHTOM to Solar System objects, as the extended and evolving coma made the interpretation of the photometry more challenging. Consequently, this experiment provided especially useful information for the future development of Solar System tools within BHTOM.

This study also demonstrated the use of BHTOM for coordinating non-sidereal observing campaigns across a diverse set of observing facilities. Although BHTOM was used here to provide uniform calibration and PSF photometry, users can either adopt the standard pipeline products or use BHTOM purely for coordination while applying independent photometric and calibration methods. If adopted, the pipeline delivers uniform calibrated photometry that can be used immediately to track brightness and color evolution and, where the data support it, to search for periodic signals. This flexibility is particularly relevant for small-body studies, where observing strategies and analysis can vary significantly between science cases. In addition, as BHTOM does not require traditional observing proposals, time-critical or target-of-opportunity observations can be requested from the facilities without the need for competitive allocation processes.

7. Conclusions

In this paper, we have presented the results from an extensive monitoring campaign of 3I/ATLAS over a 70-day observing window with data from 16 telescopes and 1554 images obtained between 2025 July 04 and 2025 September 11. Our main conclusions are as follows:

1. BHTOM was used to coordinate observations and calibrate photometric data of 3I/ATLAS obtained from the observatories within the BHTOM network, enabling consistent

time-domain analysis of a non-sidereal target beyond its standard application to sidereal sources and demonstrating its suitability for small-body science. Although PSF photometry is not optimal for quantifying the extended coma flux, it provided a uniform central-component light curve suitable for long-term activity trends and rotational analysis, and future small-body applications will preferentially adopt fixed-aperture photometry;
2. We obtained a high-cadence, multiband pre-perihelion light curve of 3I/ATLAS spanning 70 days, which exhibited a steady ∼3 magnitude decrease, consistent with gradual activity evolution and showing no evidence of anomalous or outburst-like behavior;
3. We measured the rotation period of 3I/ATLAS using detrended LCOGT multiband photometry and LS periodogram analysis, adopting a double-peaked rotation period of $P_{\rm rot} = 15.98 \pm 0.08$ h, consistent with values reported in previous studies;
4. The colors of 3I/ATLAS are statistically non-changing. The large variance of spectral slopes between $4.47 > R_h > 3.5$ au was likely driven by crowded-field photometry near the Galactic center. We found a weak, non-significant tendency for 3I/ATLAS to become bluer as activity increased at $3.5 > R_h > 2.2$ au; however, follow-up observations are required to confirm this;
5. We used aperture photometry to quantify the relative dust production rate of 3I/ATLAS using the $Af\rho$ parameter, measuring an increase in $A(0°)f\rho$ from ∼600 to 1100 cm over MJD 60 897–60 929 (UT 2025 August 10 and 2025 September 11) as the comet approached the Sun from 3.18 au to 2.19 au;
6. Under simplified assumptions for the dust properties, we measured an increase in the dust mass-loss rate from ≤217 to ≤328 kg s^{-1} over a ∼1 month observing period;
7. We measured an activity index of $n = -1.24 \pm 0.02$, with the shallow slope indicating the presence of an already well-developed dust coma with no evidence of sudden changes in the dust production rate seen in our dataset, consistent with the observed photometric behavior and visual inspection of the images.

Data availability

The photometric data used in this work are available on Zenodo via DOI: 10.5281/zenodo.19737922 under an open-source Creative Commons Attribution License.

Acknowledgements. We thank the anonymous reviewer for their useful comments and feedback, which have significantly improved this paper. A.F.G. led the writing and submission of the manuscript, scheduled the LCOGT observations, performed the data analysis, and led the overall project. Ł.W. scheduled LCOGT observations, oversaw the use of BHTOM, and provided edits and improvements to the manuscript. P.M. and K.K. were responsible for processing and calibrating the data in BHTOM. E.B. carried out the color analysis and led the writing for the corresponding section of the manuscript. C.O.C., H.H.H., M.S.P.K., and J.E.R. provided Solar System context, interpretation and manuscript feedback. P.J.P. provided meaningful BHTOM and photometry discussion. S.F. coordinated the observations from the Turkish observatories. R.E.C. and C.S. provided the observations from the Danish 1.54-metre Telescope. M.Z. provided the observations from the UZO telescope. B.H. and S.K. provided the observations from SOAB. W.B. contributed conceptually and reviewed the manuscript K.P. and D.O'N. led the GOTO observations. S.A., F.K.Y., S.Ö., M.İ., Ç.N., O.Ş., A.C.K., C.T.T. and F.T. were members of the Turkish observing teams that contributed data to this work. M.D. was the PI on the LCOGT programme. J.M. and M.W. were members of the BHTOM team M.A., C.V.A., V.B., M.J.B., A.D., R.F.J., T.C.H., M.H., E.K., F.L., P.L.P., L.M., A.M., V.M., V.O., C.O., M.R., S.S., A.S.S.M., J.S., J.S., J.T.R., and R.V. were members of the MiNDSTEp consortium. K.A., M.J.D., J.L., K.U., S.B., D.S., D.K.G., V.D., P.O'B., G.R., K.N., R.K., R.P.B., L.K.N., D.P., J.C., T.K. and A.K. were members of the GOTO collaboration. All authors provided feedback on the manuscript. A.F.G., Ł.W. and P.P. acknowledge that this work is part of a project that has received funding from the European Union's Horizon Europe Research and Innovation Programme under Grant Agreement No. 101131928 (ACME). Ł.W. acknowledges support from the Polish National Science Centre DAINA grant No. 2024/52/L/ST9/00210. This work makes use of observations from the Las Cumbres Observatory global telescope network. IST40 is one of the observational facilities of the Istanbul University Observatory, which was funded by the Scientific Research Projects Coordination Unit of Istanbul University with project numbers BAP-3685 and FBG-2017-23943. The data in this study were obtained with the T80 telescope at the Ankara University Astronomy and Space Sciences Research and Application Center (Kreiken Observatory) with project number of 25C.T80.07. TUG100 and ATA050 Telescopes at the Antalya TUG Site and Erzurum DAG Site of the Türkiye National Observatories have been utilized, and we express our gratitude for the support provided by the Türkiye National Observatories and all its staff. The Gravitational-wave Optical Transient Observer (GOTO) project acknowledges the support of the Monash-Warwick Alliance; University of Warwick; Monash University; University of Sheffield; University of Leicester; Armagh Observatory & Planetarium; the National Astronomical Research Institute of Thailand (NARIT); Instituto de Astrofísica de Canarias (IAC); University of Portsmouth; University of Turku; University of Birmingham; and the UK Science and Technology Facilities Council (STFC, grant numbers ST/T007184/1, ST/T003103/1 and ST/Z000165/1). R.F.J. acknowledges the support provided by the GEMINI/ANID project under grant number 32240028, by ANID's Millennium Science Initiative through grant ICN12_009, awarded to the Millennium Institute of Astrophysics (MAS), and by ANID's Basal project FB210003 The work presented here is supported by the Carlsberg Foundation, grant CF25-0040. The grant CF25-0040 is granted to TCH/SDU-Galaxy. L.M. acknowledges the financial contribution from the PRIN MUR 2022 project 2022J4H55R. E. Khalouei has been partially supported by the National Research Foundation of Korea (NRF) grant funded by the Korea government (MSIT) (No. RS-2024-00394623). A.M. and J.S. acknowledge support from STFC under grant number ST/Y002563/1. M.Ż. acknowledge support from program of the Polish Ministry of Science under the title 'Regional Excellence Initiative', project no. RID/SP/0050/2024/1. LINCC Frameworks is supported by Schmidt Sciences. C.O.C. gratefully acknowledges support from the NASA CSSFP (grant No. 80NSSC26K0380), and Arthur & Jeanie Chandler. C.O.C. acknowledges support from the DiRAC Institute in the Department of Astronomy at the University of Washington. The DiRAC Institute is supported through generous gifts from the Charles and Lisa Simonyi Fund for Arts and Sciences, Janet and Lloyd Frink, and the Washington Research Foundation.

References

A'Hearn, M. F., Schleicher, D. G., Millis, R. L., Feldman, P. D., & Thompson, D. T. 1984, AJ, 89, 579
Alarcon, M. R., Serra-Ricart, M., Licandro, J., et al. 2025, Astronomer's Telegram, 17264, 1
Andersen, J., Andersen, M. I., Klougart, J., et al. 1995, Messenger, 79, 12
Bellm, E. C., Kulkarni, S. R., Graham, M. J., et al. 2019, PASP, 131, 018002
Belyakov, M., Fremling, C., Graham, M. J., et al. 2025, RNAAS, 9, 194
Bertin, E. 2006, in Astronomical Society of the Pacific Conference Series, 351, Astronomical Data Analysis Software and Systems XV, eds. C. Gabriel, C. Arviset, D. Ponz, & S. Enrique, 112
Bertin, E., & Arnouts, S. 1996, A&AS, 117, 393
Bessell, M., & Murphy, S. 2012, PASP, 124, 140
Bolin, B. T., Belyakov, M., Fremling, C., et al. 2025, MNRAS, 542, L139
Brown, T. M., Baliber, N., Bianco, F. B., et al. 2013, PASP, 125, 1031
Bufanda, E., Meech, K. J., Kleyna, J. T., et al. 2023, PSJ, 4, 2
Chambers, K. C., Magnier, E. A., Metcalfe, N., et al. 2016, arXiv e-prints [arXiv:1612.05560]
Champagne, C., McClure, L., Emery, J., et al. 2025, Astronomer's Telegram, 17283, 1
Chandler, C. O., Bernardinelli, P. H., Jurić, M., et al. 2026, ApJ, 1001, L35
Cordiner, M. A., Roth, N. X., Kelley, M. S. P., et al. 2025, ApJ, 991, L43
de León, J., Licandro, J., de la Fuente Marcos, C., et al. 2020, MNRAS, 495, 2053
de la Fuente Marcos, R., Alarcon, M. R., Licandro, J., et al. 2025, A&A, 700, L9
Delsanti, A., Hainaut, O., Jourdeuil, E., et al. 2004, A&A, 417, 1145
Denneau, L., Siverd, R., Tonry, J., et al. 2025, Minor Planet Electronic Circulars, 2025-N12
Fink, U. 2009, Icarus, 201, 311
Fink, U., & Rubin, M. 2012, Icarus, 221, 721
Fitzsimmons, A., Snodgrass, C., Rozitis, B., et al. 2018, Nat. Astron., 2, 133
Fitzsimmons, A., Hainaut, O., Meech, K. J., et al. 2019, ApJ, 885, L9

Fitzsimmons, A., Meech, K., Matrà, L., & Pfalzner, S. 2024, in Comets III, eds. K. J. Meech, M. R. Combi, D. Bockelée-Morvan, S. N. Raymodn, & M. E. Zolensky, 731
Fornasier, S., Mottola, S., Keller, H. U., et al. 2016, Science, 354, 1566
Frincke, T. T., Yaginuma, A., Noonan, J. W., et al. 2026, MNRAS, 545, staf1994
Gaia Collaboration (Prusti, T., et al.) 2016, A&A, 595, A1
Gaia Collaboration (Montegriffo, P., et al.) 2023a, A&A, 674, A33
Gaia Collaboration (Vallenari, A., et al.) 2023b, A&A, 674, A1
Garcia, R. S., & Gil-Hutton, R. 2021, Planet. Space Sci., 206, 105308
Gardener, D., Snodgrass, C., & Ligier, N. 2022, MNRAS, 517, 4305
Gillan, A. F., Fitzsimmons, A., Denneau, L., et al. 2024, PSJ, 5, 25
Gillan, A. F., Fitzsimmons, A., Denneau, L., et al. 2025, PSJ, 6, 172
Ginsburg, A., Sipőcz, B. M., Brasseur, C. E., et al. 2019, AJ, 157, 98
Giorgini, J. D., Yeomans, D. K., Chamberlin, A. B., et al. 1996, Am. Astron. Soc., 28, 25.04
Guzik, P., Drahus, M., Rusek, K., et al. 2020, Nat. Astron., 4, 53
Hodgkin, S. T., Harrison, D. L., Breedt, E., et al. 2021, A&A, 652, A76
Hopkins, M. J., Bannister, M. T., & Lintott, C. 2025a, AJ, 169, 78
Hopkins, M. J., Dorsey, R. C., Forbes, J. C., et al. 2025b, ApJ, 990, L30
Hoogendam, W. B., Kuesters, D., Shappee, B. J., et al. 2026, Open J. Astrophys., 9, 65099
Ivanova, O., Reshetnyk, V., Skorov, Y., et al. 2018, Icarus, 313, 1
Ivezić, Ž., Kahn, S. M., Tyson, J. A., et al. 2019, ApJ, 873, 111
Jewitt, D., & Luu, J. 2019, ApJ, 886, L29
Jewitt, D., & Luu, J. 2025a, Astronomer's Telegram, 17263, 1
Jewitt, D., & Luu, J. 2025b, ApJ, 994, L3
Jewitt, D., Luu, J., Rajagopal, J., et al. 2017, ApJ, 850, L36
Jewitt, D., Hui, M.-T., Kim, Y., et al. 2020, ApJ, 888, L23
Jewitt, D., Hui, M.-T., Mutchler, M., Kim, Y., & Agarwal, J. 2025, ApJ, 990, L2
Jordi, C., Gebran, M., Carrasco, J. M., et al. 2010, A&A, 523, A48
Kalberla, P. M. W., & Kerp, J. 2009, ARA&A, 47, 27
Karaali, S., Bilir, S., & Tunçel, S. 2005, PASA, 22, 24
Kareta, T., Champagne, C., McClure, L., et al. 2025, ApJ, 990, L65
Kelley, M. S., Woodward, C. E., Gehrz, R. D., Reach, W. T., & Harker, D. E. 2017, Icarus, 284, 344
Kokotanekova, R., Snodgrass, C., Lacerda, P., et al. 2017, MNRAS, 471, 2974
Kolokolova, L., Nagdimunov, L., A'Hearn, M., King, A., & Wolff, M. 2016, Planet. Space Sci., 133, 76
Li, J.-Y., A'Hearn, M. F., Belton, M. J. S., et al. 2007, Icarus, 191, 161
Li, J.-Y., Besse, S., A'Hearn, M. F., et al. 2013, Icarus, 222, 559
Licandro, J., Serra-Ricart, M., Oscoz, A., Casas, R., & Osip, D. 2000, AJ, 119, 3133
Lisse, C. M., Bach, Y. P., Bryan, S., et al. 2025, RNAAS, 9, 242
Lomb, N. R. 1976, Ap&SS, 39, 447
Lupton, R. 2005, Transformations between SDSS magnitudes and UBVRcIc, http://classic.sdss.org/dr4/algorithms/sdssUBVRITransform.html#Lupton2005
Martinez-Palomera, J., Tuson, A., Hedges, C., et al. 2025, ApJ, 994, L51
Mazzotta Epifani, E., Perna, D., Di Fabrizio, L., et al. 2014, A&A, 561, A6
McCully, C., Volgenau, N. H., Harbeck, D.-R., et al. 2018, SPIE Conf. Ser., 10707, 107070K
Meech, K. J., Belton, M. J. S., Mueller, B. E. A., Dicksion, M. W., & Li, H. R. 1993, AJ, 106, 1222
Meech, K. J., Schambeau, C. A., Sorli, K., et al. 2017a, AJ, 153, 206
Meech, K. J., Weryk, R., Micheli, M., et al. 2017b, Nature, 552, 378
Micheli, M., Farnocchia, D., Meech, K. J., et al. 2018, Nature, 559, 223
Mikolajczyk, P. J., Zieliński, P., Wyrzykowski, L., Krawczyk, A., & Kotysz, K. 2025, in Revista Mexicana de Astronomia y Astrofisica Conference Series, 59, Revista Mexicana de Astronomia y Astrofisica Conference Series, 167
Minev, M., Kostov, A., & Mutafov, A. 2025, Astronomer's Telegram, 17275, 1
Monet, D. G., Levine, S. E., Canzian, B., et al. 2003, AJ, 125, 984
Opitom, C., Fitzsimmons, A., Jehin, E., et al. 2019, A&A, 631, L8
Opitom, C., Snodgrass, C., Jehin, E., et al. 2025, MNRAS, 544, L31
Reyniers, M., Degroote, P., Bodewits, D., Cuypers, J., & Waelkens, C. 2009, A&A, 494, 379
Rodgers, C. T., Canterna, R., Smith, J. A., Pierce, M. J., & Tucker, D. L. 2006, AJ, 132, 989
Rosenbush, V., Kleshchonok, V., Ivanova, O., et al. 2026, Icarus, 444, 116799
Santana-Ros, T., Ivanova, O., Mykhailova, S., et al. 2025, A&A, 702, L3
Scargle, J. D. 1982, ApJ, 263, 835
Scarmato, T. 2025, arXiv e-prints [arXiv:2512.22365]
Schleicher, D. 2010, Composite Dust Phase Function for Comets
Schwamb, M. E., Jones, R. L., Yoachim, P., et al. 2023, ApJS, 266, 22
Seligman, D. Z., Micheli, M., Farnocchia, D., et al. 2025, ApJ, 989, L36
Serra-Ricart, M., Licandro, J., & Alarcon, M. R. 2026, A&A, 705, L3
Skrutskie, M. F., Cutri, R. M., Stiening, R., et al. 2006, AJ, 131, 1163
Snodgrass, C., Tubiana, C., Bramich, D. M., et al. 2013, A&A, 557, A33
Snodgrass, C., A'Hearn, M. F., Aceituno, F., et al. 2017, Philos. Trans. Roy. Soc. Lond. A, 375, 20160249
Solontoi, M., Ivezić, Ž., Jurić, M., et al. 2012, Icarus, 218, 571
Steeghs, D., Galloway, D. K., Ackley, K., et al. 2022, MNRAS, 511, 2405
Stetson, P. B. 1987, PASP, 99, 191
Street, R. A., Bowman, M., Saunders, E. S., & Boroson, T. 2018, SPIE Conf. Ser., 10707, 1070711
Tonry, J. L., Denneau, L., Flewelling, H., et al. 2018a, ApJ, 867, 105
Tonry, J. L., Denneau, L., Heinze, A. N., et al. 2018b, PASP, 130, 064505
Tubiana, C., Rinaldi, G., Güttler, C., et al. 2019, A&A, 630, A23
VanderPlas, J. T. 2018, ApJS, 236, 16
Weiler, M. 2018, A&A, 617, A138
Williams, G. V., Sato, H., Sarneczky, K., et al. 2017, Central Bureau Electronic Telegrams, 4450, 1
Wyrzykowski, L. 2024, in What Was That? – Planning ESO Follow up for Transients, Variables, and Solar System Objects in the Era of LSST, 4
Xing, Z., Oset, S., Noonan, J., & Bodewits, D. 2025, ApJ, 991, L50
Yang, B., Meech, K. J., Connelley, M., Zhao, R., & Keane, J. V. 2025, ApJ, 992, L9
Ye, Q., Kelley, M. S. P., Hsieh, H. H., et al. 2025, ApJ, 993, L31
Zacharias, N., Finch, C. T., Girard, T. M., et al. 2013, AJ, 145, 44
Zacharias, N., Finch, C., Subasavage, J., et al. 2015, AJ, 150, 101

[1] Astrophysics Division, National Centre for Nuclear Research, Pasteura 7, 02-093 Warsaw, Poland
[2] Astronomical Observatory, University of Warsaw, Al. Ujazdowskie 4, 00-478 Warsaw, Poland
[3] European Astronomical Society of Small Telescopes (EASST.eu)
[4] Astronomical Institute, University of Wrocław, ul. Mikołaja Kopernika 11, 51-622 Wrocław, Poland
[5] Institute for Astronomy, University of Edinburgh, Royal Observatory, Edinburgh EH9 3HJ, UK
[6] Dept. of Astronomy & the DiRAC Institute, University of Washington, 3910 15th Ave NE, Seattle, WA 98195, USA
[7] LSST Interdisciplinary Network for Collaboration and Computing Frameworks, 933 N. Cherry Avenue, Tucson, AZ 85721, USA
[8] Dept. of Astronomy & Planetary Science, Northern Arizona University, PO Box 6010, Flagstaff, AZ 86011, USA
[9] Department of Astronomy and Space Sciences, Faculty of Science, Istanbul University, 34116 Istanbul, Türkiye
[10] Istanbul University Observatory Research and Application Center, 34116 Istanbul, Türkiye
[11] Planetary Science Institute, 1700 East Fort Lowell Road, Suite 106, Tucson, AZ 85719, USA
[12] Department of Astronomy, University of Maryland, College Park, MD 20742-0001, USA
[13] Max Planck Institute for Solar System Research, 37077 Göttingen, Germany
[14] Centre for Exoplanet Science, SUPA School of Physics & Astronomy, University of St Andrews, North Haugh, St Andrews KY16 9SS, UK
[15] Astronomical Observatory, Jagiellonian University, ul. Orla 171, 30-244, Kraków, Poland
[16] Astrophysics Group, Keele University, Staffordshir, ST5 5BG, UK
[17] Ankara University, Faculty of Science, Astronomy & Space Sciences Department, Tandogan, 06100 Ankara, Türkiye
[18] Ankara University, Astronomy and Space Sciences Research and Application Center (Kreiken Observatory), İncek Blvd., 06837 Ahlatlıbel, Ankara, Türkiye
[19] Türkiye National Observatories, TUG, 07070 Antalya, Türkiye
[20] School of Physics and Astronomy, University of Birmingham, Birmingham B15 2TT, UK
[21] School of Physics and Astronomy, Monash University, Clayton, VIC 3800, Australia
[22] Türkiye National Observatories, DAG, 25050 Erzurum, Türkiye
[23] Atatürk University, Institute of Science, Department of Astronomy and Astrophysics, 25240 Erzurum, Türkiye
[24] Isaac Newton Group of Telescopes, Apartado 321, 38700 Santa Cruz de La Palma, Spain
[25] Janusz Gil Institute of Astronomy, University of Zielona Gora, Szafrana 2, 65-516 Zielona Gora, Poland

[26] Department of Physics, University of Warwick, Gibbet Hill Road, Coventry CV4 7AL, UK
[27] Niels Bohr Institute, Øster Voldgade 5, 1350 Copenhagen, Denmark
[28] Centro de Astronomía, Universidad de Antofagasta, Av. Angamos 601, Antofagasta, Chile
[29] Dipartimento di Fisica "E.R. Caianiello", Università di Salerno, Via Giovanni Paolo II 132, 84084 Fisciano, Italy
[30] Istituto Nazionale di Fisica Nucleare, Sezione di Napoli, Napoli, Italy
[31] Jodrell Bank Centre for Astrophysics, Department of Physics and Astronomy, The University of Manchester, Manchester M13 9PL, UK
[32] Earth System Sciences, Atmospheric Science, University of Hamburg, Hamburg, Germany
[33] Instituto de Astrofísica de Canarias, 38205 La Laguna, Tenerife, Spain
[34] Department of Physics and Astronomy, University of Sheffield, Sheffield S3 7RH, UK
[35] Instituto de Astronomia y Ciencias Planetarias, Universidad de Atacama, Copayapu 485, Copiapo, Chile
[36] Millennium Institute of Astrophysics MAS, Nuncio Monsenor Sotero Sanz 100, Of. 104, Providencia, Santiago, Chile
[37] Instituto de Astrofísica, Facultad de Física, Pontificia Universidad Católica de Chile, Av. Vicuña Mackenna 4860, 7820436, Macul, Santiago, Chile
[38] University of Southern Denmark, Department of Physics, Chemistry and Pharmacy, SDU-Galaxy, Campusvej 55, 5230, Odense M, Denmark
[39] Astronomisches Rechen-Institut, Zentrum für Astronomie der Universität Heidelberg (ZAH), 69120 Heidelberg, Germany
[40] Department of Physics, Ewha Womans University, 52 Ewhayeodae-gil, Seodaemun-gu, Seoul 03760, Republic of Korea
[41] Department of Physics & Astronomy, University of Turku, Vesilinnantie 5, 20014 Turku, Finland
[42] Centre for Electronic Imaging, Department of Physical Sciences, The Open University, Milton Keynes MK7 6AA, UK
[43] INAF – Turin Astrophysical Observatory, via Osservatorio 20, 10025 Pino Torinese, Italy
[44] Department of Physics, University of Rome "Tor Vergata", Via della Ricerca Scientifica 1, 00133 Rome, Italy.
[45] National Astronomical Research Institute of Thailand, Chiangmai 50180, Thailand
[46] Institute of Cosmology & Gravitation, University of Portsmouth, Portsmouth PO1 3FX, UK
[47] School of Physics & Astronomy, University of Leicester, University Road, Leicester LE1 7RH, UK
[48] Departamento de Matemática y Física Aplicadas, Facultad de Ingeniería, Universidad Católica de la Santísima Concepción, Alonso de Rivera 2850, Concepción, Chile
[49] Armagh Observatory & Planetarium, College Hill, Armagh BT61 9DG, UK
[50] Department of Astrophysics, Cosmology and Fundamental Interactions, Brazilian Center for Research in Physics, Centro Brasileiro de Pesquisas Físicas, Brazil
[51] Department of Physics, Isfahan University of Technology, Isfahan 84156-83111, Iran

Appendix A: Observing log table

Table A.1: This table shows the observatories, telescopes, number of exposures in each filter, the start and end date of observation for individual telescopes in both UT and MJD, and the number of unique nights of observation.

Observatory	Telescope	No. observations × Filter(s)	Range of observation dates	MJD	No. nights
LCOGT-Siding Spring Observatory	0.4 m	$11 \times g'$, $36 \times r'$, $9 \times i'$	2025 July 07 – 2025 Aug. 27	60863 – 60914	14
LCOGT-Siding Spring Observatory	1 m	$5 \times g'$, $15 \times r'$, $5 \times i'$	2025 Aug. 12 – 2025 Aug. 26	60899 – 60913	5
LCOGT-SAAO	0.4 m	$11 \times g'$, $33 \times r'$, $11 \times i'$	2025 July 14 – 2025 Sept. 2	60870 – 60920	12
LCOGT-SAAO	1 m	$13 \times g'$, $43 \times r'$, $12 \times i'$	2025 July 19 – 2025 Sept. 11	60875 – 60929	17
LCOGT-Teide Observatory	1 m	$1 \times g'$, $3 \times r'$, $1 \times i'$	2025 July 30	60886	1
LCOGT-CTIO	0.4 m	$25 \times g'$, $72 \times r'$, $19 \times i'$	2025 July 05 – 2025 Sept. 06	60861 – 60924	26
LCOGT-CTIO	1 m	$17 \times g'$, $50 \times r'$, $14 \times i'$	2025 July 14 – 2025 Sept. 11	60870 – 60929	19
LCOGT-Haleakala Observatory	0.4 m	$20 \times g'$, $53 \times r'$, $18 \times i'$	2025 July 20 – 2025 Aug. 27	60876 – 60914	20
† SOAB	0.4 m	$8 \times R$, $5 \times I$	2025 July 04 – 2025 July 23	60860 – 60879	3
† Türkiye National Observatories	1 m (TUG100)	$19 \times r'$, $73 \times i'$, $26 \times z'$	2025 July 11	60867	1
† Ankara University Kreiken Observatory	0.8 m (T80)	$4 \times g'$, $32 \times r'$, and $14 \times i'$	2025 July 7	60863	1
† Türkiye National Observatories	0.5 m (ATA050)	$9 \times R$	2025 July 7	60863	1
† Istanbul University Observatory	0.4 m (IST40)	$70 \times R$	2025 July 18 – 2025 July 27	60874 – 60883	6
UZO	0.5 m	$157 \times B$, $249 \times V$, $250 \times R$	2025 July 17 – 2025 July 24	60873 – 60880	5
La Silla Observatory	Danish 1.54 m Telescope	$32 \times B$, $35 \times V$, $35 \times R$, $31 \times I$	2025 July 16 – 2025 July 29	60872 – 60885	3
Siding Spring Observatory	0.4 m (GOTO)	$8 \times L$	2025 Aug. 17 – 2025 Aug. 23	60904–60910	4

Notes. g', r', i', and z' correspond to the Sloan filters, B, V, R, and I correspond to the J-C filter system, and L corresponds to the GOTO L-band. † represents the images that were binned by night.

Appendix B: UZO light curves

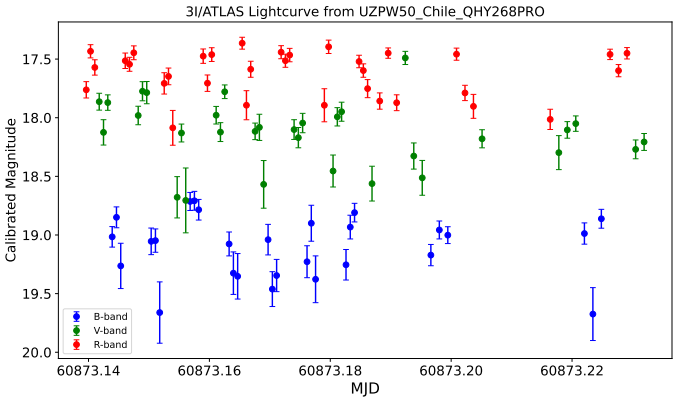


Fig. B.1: The calibrated GaiaSP magnitude vs time in MJD on MJD 60873 for 2.1 hours. The blue, green and red points represent the J-C B, V and R bands.

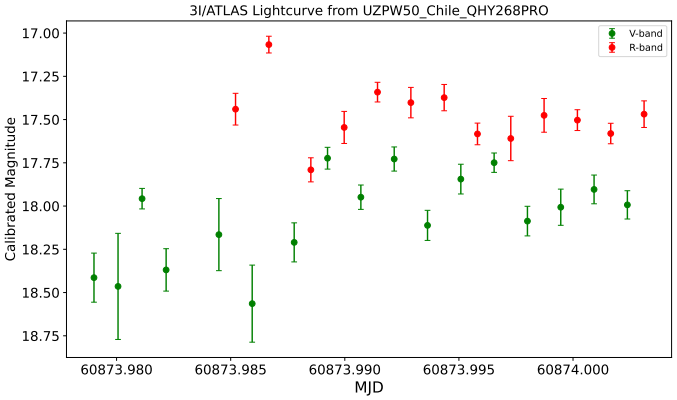


Fig. B.2: The calibrated GaiaSP magnitude vs time in MJD on MJD 60873 and 60874 for 0.4 hours. The green and red points represent the J-C V and R bands.

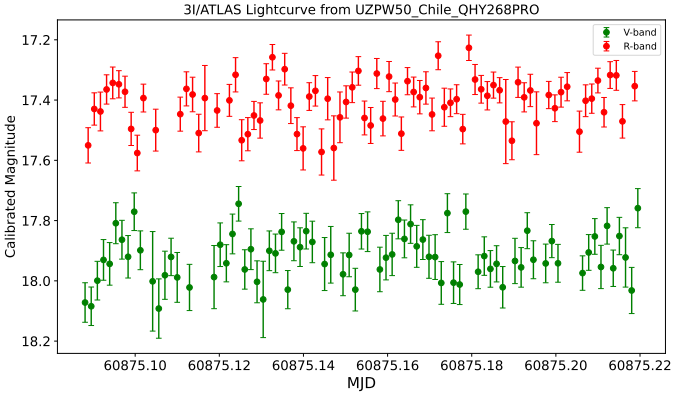


Fig. B.3: The calibrated GaiaSP magnitude vs time in MJD on MJD 60875 for 2.8 hours. The blue, green and red points represent the J-C V and R bands.

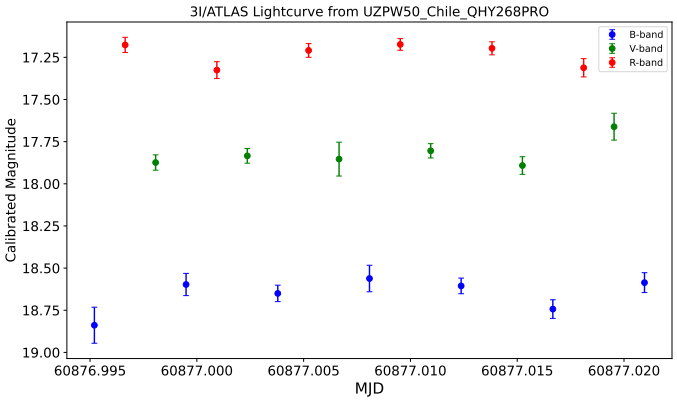


Fig. B.4: The calibrated GaiaSP magnitude vs time in MJD on MJD 60876 and 60877 for 0.6 hours. The blue, green and red points represent the J-C B, V and R bands.

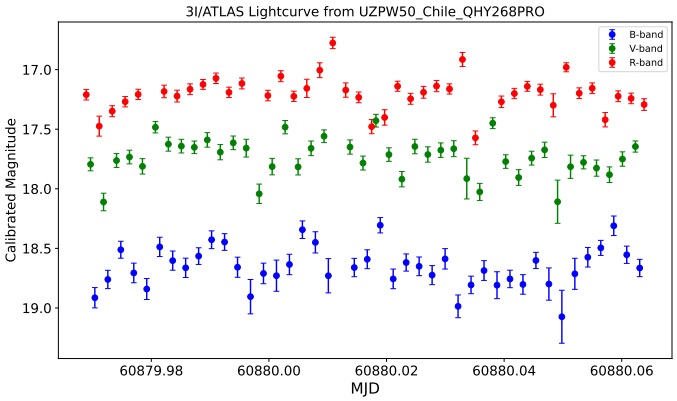


Fig. B.5: The calibrated GaiaSP magnitude vs time in MJD on MJD 60879 and 60880 for 2 hours. The blue, green and red points represent the J-C B, V and R bands.

Appendix C: Danish 1.54 m Telescope light curves

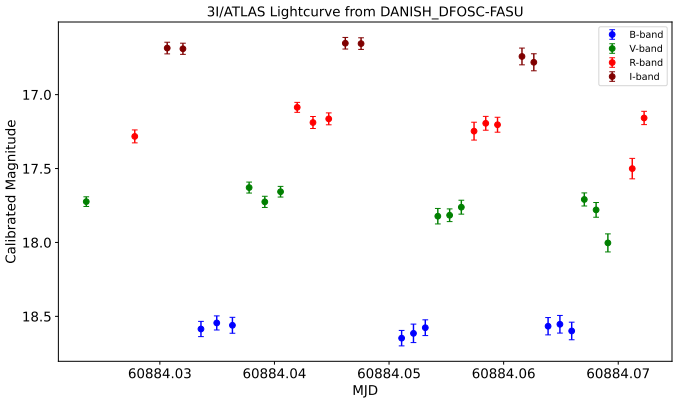


Fig. C.1: The calibrated GaiaSP magnitude vs time in MJD on MJD 60884 for 0.7 hours. The blue, green, red and maroon points represent the J-C B, V, R and I bands.

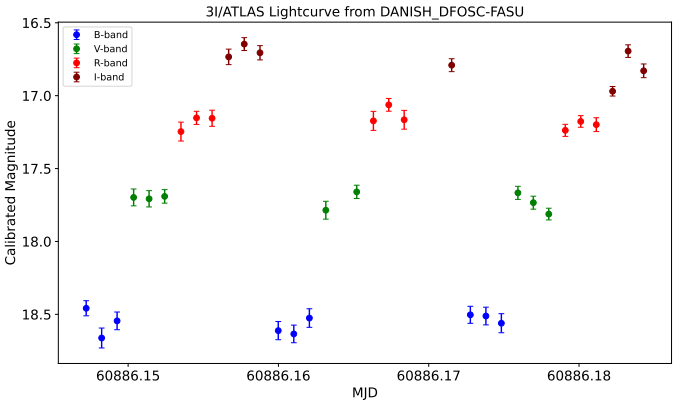


Fig. C.2: The calibrated GaiaSP magnitude vs time in MJD on MJD 60886 for 0.9 hours. The blue, green, red and maroon points represent the J-C B, V, R and I bands.